UNIVERSITY OF CALIFORNIA
RIVERSIDE

Dust Delivery and Accumulation of Highly Reactive Iron in the Atlantic Ocean and its Biological Implications

A Thesis submitted in partial satisfaction
of the requirements for the degree of

Master of Science

in

Geological Sciences

by

Bridget Kimhaejin Lee

December 2015

Thesis Committee:
Dr. Timothy Lyons, Chairperson
Dr. Robert Allen
Dr. Gordon Love
Dr. Jeremy Owens

The Thesis of Bridget Kimhaejin Lee is approved:

_____

_____

_____

Committee Chairperson

University of California, Riverside

ACKNOWLEDGEMENTS

Firstly, I would like to express my sincere gratitude to my advisor Prof. Tim Lyons for the continuous support of my M.S. for his patience, motivation, and immense knowledge. His guidance helped me in all the time of research and writing of this thesis.

Besides my advisor, I would like to thank the rest of my thesis committee: Prof. Gordon Love, Prof. Robert Allen and Prof. Jeremy Owens for their insightful comments and encouragement.

My sinciere thanks go to Prof. Pete Sadler and Prof. Robert Raiswell for their precious support.

I thank my fellow graduate students (Konstantin Choumiline, Charles Diamond, Caroline Gott, Leanne Hancock, Dalton Hardisty and Stephanie Olson), research manager (Steve Bates) and research technician (Andrew Robinson) for working together before deadlines and discussing new ideas.

I acknowledge the Integrated Ocean Drilling Program (IODP) and the core repository for providing the samples used in this study.

Last but not the least, I would like to thank my family: my husband William and my two little boys Jonathan and Steve for endless encouragement and support. Jonathan and Steve, thank you for sacrificing your weekend and playtime to come to work with mommy and make the Earth Science court yard your playground.

ABSTRACT OF THE THESIS

Dust Delivery and Accumulation of Highly Reactive Iron in the Atlantic Ocean and its Biological Implications

by

Bridget Kimhaejin Lee

Master of Science, Graduate Program in Geological Sciences
University of California, Riverside, December 2015
Dr. Timothy Lyons, Chairperson

Dissolved iron is an essential micronutrient for marine phytoplankton, and its availability has controlled patterns of primary productivity and carbon cycling throughout Earth history. Iron, although abundant in the Earth's crust, is present at low concentrations in seawater today and is a limiting nutrient for phytoplankton. Aeolian (wind blown) dust (loess) is a major source of this micronutrient to the ocean, and its deposition has important implications for the global CO_2 budget. In this study, I explore distributions of potentially bioavailable Fe, the soluble fraction required by phytoplankton for photosynthesis and nitrogen assimilation, in deep-sea sediments in the North and South Atlantic Oceans. I used a state-of-the-art Fe speciation technique to characterize Fe inputs from different source regions, specifically North Africa and Patagonia, to address the patterns and their implications across spatial gradients and glacial-interglacial time scales.

In many open-ocean regions, the input of new iron to the surface waters is dominated by atmospheric deposition of soluble iron in aeolian dust. Multiple records

have shown dust accumulation is correlated with glacial-interglacial cycles, with glacial periods being substantially dustier. Furthermore, the delivery of aeolian dust to the North and South Atlantic Oceans are from two very different source regions and soil types. With this framework, I analyzed a total of five IODP cores from these two regions, and my preliminary data show similar patterns of iron distribution from both the North and South Atlantic Oceans. Furthermore, while total dust accumulation varies dramatically on glacial-interglacial time scales, I have found no pattern in the reactivity of the dust-associated Fe across the same interval. I have also analyzed a range of sediment grain sizes to isolate the dust-dominated fraction and found no size effects in the distribution of bioavailable iron. There is, however, a trend of decreasing ratios of highly reactive (oxide iron that is/was potentially bioavailable) to total iron (Fe_{HR}/Fe_T) with greater distance from the source region. This trend might reflect increased reactivity (likely through prolonged atmospheric/cloud processing) during long-range transport and subsequent loss of soluble Fe in the water column. This lost iron could have simulated primary production in the surface ocean even (or preferentially) at great distances from the source region. If correct, these data suggest lower dust fluxes but with proportionally more reactive iron with increasing distance from the source. Remaining challenges include a better understanding of the role of deep-water dust dissolution and enhanced solubility linked specifically to low oxygen conditions in the water column and sediments. The latter could be a positive feedback tied to high primary production and associated oxygen demand.

TABLE OF CONTENTS

LIST OF FIGURES

Introduction

Iron is the fourth most abundant element in the Earth's crust and an essential nutrient for all living organisms. Despite its abundance in the environment, Fe is found in low concentrations in the ocean today due to the low solubility of Fe under oxidizing conditions and is a limiting nutrient for primary productivity in many regions of the ocean. [*Boyd et al.*, 2000; *Martin*, 1990; *Watson et al.*, 2000]. Iron limitation occurs in high nutrient-low chlorophyll (HNLC) regions such as Southern Atlantic, equatorial Pacific and subarctic Pacific regions of the ocean [*Boyd et al.*, 2000; *Boyd et al.*, 2004; *Coale et al.*, 1996; *Martin et al.*, 1994].

Iron is delivered to the open ocean mainly by rivers, aeolian dust, icebergs, subglacial runoff, hydrothermal activity and by recycling from shelf sediments. [*S. W. Poulton and Raiswell*, 2002]. Rivers and hydrothermal activity supply iron in a dissolved form, but neither source is effective at reaching surface waters due to removal of dissolved iron from rivers in estuaries; hydrothermal inputs are mostly limited to the deep ocean. The main input of Fe to the surface open ocean is atmospheric deposition, mostly of aluminosilicate minerals in dust from arid and semiarid regions [*Balsam et al.*, 1995; *Conway and John*, 2014; *Duce and Tindale*, 1991]. Therefore, changes in atmospheric dust flux affect the concentration of bioavailable Fe in the upper ocean. Upwelling and vertical mixing of deep water can also bring Fe to the surface waters. However, in an overall sense, the amount of Fe delivered by dust exerts a major control on the amount of available in the ocean.

Aeolian dust is a major driver in the global climate system through its influence

on the oceanic biogeochemical cycles of carbon and nutrients through the coupled delivery of micronutrients like iron [*Baker et al.*, 2003; *Fung et al.*, 2000; *Jickells et al.*, 2005; *Sarthou et al.*, 2003]. The ocean receives dust-containing iron as fine-grained iron oxides and oxyhydroxides mostly as grain coatings and as silicate phases. Iron is required for photosynthesis and nitrogen assimilation in these organisms. Also, because of its role as an enzymatic cofactor in nitrogenase, iron deficiencies can limit the extent of nitrogen fixation in the portions of the surface ocean. The equatorial Pacific Ocean, subarctic Pacific Ocean and the Southern Atlantic Ocean are the major high nitrate-low chlorophyll (HNLC) areas today, totaling 20% of present open ocean [*Aumont et al.*, 2003; *N M Mahowald et al.*, 2009; *J. Keith Moore et al.*, 2004]. Additionally, in tropical and subtropical regions, iron deficiency may also limit phytoplankton growth in subtropical gyres [*Bergquist and Boyle*, 2006; *Johnson et al.*, 1997; *Martin et al.*, 1994; *Tortell et al.*, 1999], as well as nitrogen fixation by diazotrophs that contain iron-molybdenum nitrogenase systems [*Berman-Frank et al.*, 2001; *Falkowski*, 1997; *C M Moore et al.*, 2009]. Thus, Fe in aeolian dust can directly and indirectly limit primary productivity for large portions of the world ocean, thereby affecting biological carbon export at the global scale [*Arrigo*, 2005; *Gregg et al.*, 2003; *Jickells et al.*, 2005; *N M Mahowald et al.*, 2009; *J. Keith Moore et al.*, 2001; *Rea*, 1994].

Paleo-dust records have shown that accumulation is correlated with glacial-interglacial cycles. Glacial periods are substantially dustier, with dust fluxes two to five times greater than during interglacial periods [*Andersen et al.*, 1998; *Kohfeld and Harrison*, 2001]. In addition, during glacial times, low sea level exposes costal

sediments, and these unconsolidated deposits have potential to become a major source of dust. The "Iron Hypothesis" proposed by Martin et al. (1990) attributes decreased atmospheric CO_2 concentrations during glacial times to increased iron deposition by aeolian input that stimulated increased primary production in the ocean. Here, I examine dust deposition and its implications in primary production across glacial and interglacial cycles and geographically at locations close to and far from the source regions.

2. Bioavailable Iron

Iron occurs in two valence states: oxidized ferric iron, Fe (III), and reduced ferrous iron, Fe (II). Not all iron is bioavailable in the ocean. Soluble iron is considered to be available for biological uptake, but other forms of iron may also be bioavailable, such as ferrihydrite and goethite in nanoparticulate clusters. The most important mineralogical influence is the solubility of nanoparticulate Fe oxyhydroxides (particularly ferrihydrite) [*Robert Raiswell and Canfield*, 2012; *R. Raiswell et al.*, 2008]. Ferrihydrite is thermodynamically the least stable iron oxyhydroxide in seawater and is the most likely source of bioavailable Fe [*Rob Raiswell*, 2011]. However, its aggregation, growth or transformation to more geologically stable phases (e.g., goethite and hematite) can decrease its bioavailability by decreasing its solubility and rates of dissolution, and these processes can occur rapidly. In addition, the rates of bioavailable Fe supply from ferrihydrite to the oceans can be influenced by disaggregation, photochemical reduction and siderophore-aided dissolution [*Hand et al.*, 2004; *Journet et al.*, 2008; *Mackie et al.*, 2005; *Rubasinghege et al.*, 2010; *Spokes et al.*, 1994; *Zhu et al.*, 1997].

More generally, Fe_{HR} and thus potentially bioavailable iron oxyhydroxides reach the oceans from rivers, glacial delivery, atmospheric dust, hydrothermal activity, coastal erosion and diagenetic recycling from the shelves [*Fan et al.*, 2006; *Rob Raiswell et al.*, 2006]. However, the main source of bioavailable Fe to the open oceans is the aeolian dust, thus the emphasis on that fraction in this study. Past studies also interested in delivery of potentially bioreactive Fe to the ocean have relied on analytical protocols that initiated with isolation of the dust fraction from the bulk sediments but in the process removed substantial portions of the potentially or formerly soluble Fe through chemical processing in the lab. These steps involved chemical leaching, including HCl, which is effective at removing even well crystallized iron oxides [*Berner*, 1970; *Leventhal and Taylor*, 1990; *Robert Raiswell and Canfield*, 1998; *R Raiswell et al.*, 1994]. In this study, I have adopted a wet chemical extraction of iron phases in sediments not pre-treated chemically, thus preserving the most reactive forms and their diagenetic products [*Simon W. Poulton and Canfield*, 2005]. Importantly, substantial portions of these Fe oxides and oxyhydroxides may have formed from mineralogical transformations of soluble bioavailable precursor phases following deposition [*Benner et al.*, 2002; *De Vitre et al.*, 1993]. As such, they might function as proxies for the potential initial pools of reactive mineralogies. As such, they might function as proxies for the potential initial pools of reactive mineralogies. Although not a perfect approach, this is a significant step forward from a past emphasis on total iron—often in pretreated samples. Details and further justification are provided below.

3. Material and Methods

3.1 Study Areas and Dust Sources

The five sample locations were strategically selected to provide a wide spatial distribution, with four in the Northern and one in Southern Atlantic Ocean (Fig. 1). The northern sites represent both proximal and distal locations relative to their dominant source region in northern Africa. Samples used for this study were obtained from the Deep Sea Drilling Project (DSDP) and Ocean Drilling Program (ODP) archived in the Gulf Coast Repository, United States (site 1091), and the Bremen Repository, Germany (sites 1062, 1063, 1074, 659).

Site 1091, ODP Leg 177, is located on the western flank of the Meteor Rise in the Atlantic Ocean. It has played an important role in investigations of the Fe hypotheses [*Boyd et al.*, 2000] as linked to glacial-interglacial variations in biological productivity, as well as for reconstructing the history of the Polar Front in the Southern Ocean. This site is located in the central Polar Front Zone (PFZ), and due to its proximity to the PFZ, the sedimentary environment is highly sensitive to changes of the frontal position [*Kleiven and Jansen*, 2003]. Site 1091 has a water depth of 4363 m and lies within lower Circumpolar Deep Water (CDW) [*Gersonde et al.*, 1999]. During glacial periods, opal accumulation rates increase, whereas carbonate export production and preservation decline [*Etourneau et al.*, 2012]. Maximum biological productivity occurred within the PFZ during the last glaciation, and it was presumably sustained by iron fertilization of surface water [*Kumar et al.*, 1995]. Iron delivered by enhanced aeolian dust input was mainly from the Patagonian desert.

Sites 1062 and 1063 were sampled in the North Atlantic Ocean as part of ODP Leg 172 and yielded records of rapid changes in climate and ocean circulation during the middle Pliocene to Pleistocene [Lund et al., 2001]. These sites occur within sediment drifts of the western North Atlantic Ocean: the Bahamas Outer Ridge (Site1062) and the Bermuda Rise (Site 1063) [Keigwin and Jones, 1989]. These sites also lie within the region of Saharan dust transport over the North Atlantic Ocean and have bulk deposition rates of approximately 4.5-6.2 $\times 10^4$ μg m^{-2} yr^{-1} [Arimoto et al., 2003; Bacon and Rosholt, 1982; Jickells et al., 2005; Neff et al., 2002].

Site 659 is from ODP expedition 108 located at a water depth of 3070 m on top of the Cape Verde Plateau near the northwest African continental margin. This site permits study of sediment in a non-upwelling area with high average carbonate concentrations [*Mienert and Schultheiss*, 1986]. Sediment compositions are influenced by biological productivity in the cold-water front of the Canary Eastern boundary current and by transport of aeolian dust from the Sahara Desert [*Sarnthein et al.*, 1982].

Core 174B from ODP site 1074 was collected in the North Pond area (an isolated sediment 'pond') on the western flank of the Mid-Atlantic Ridge [*Hirano et al.*]. The sediments are enriched in Fe near the top and bottom of the sediment pile [*Türke et al.*]. This region receives dust from the Sahara Desert, and the sediment is broadly characterized as nannofossil-rich pelagic accumulation containing varying amounts of clay, foraminifers and Mn micro-nodules [*Ziebis et al.*, 2012].

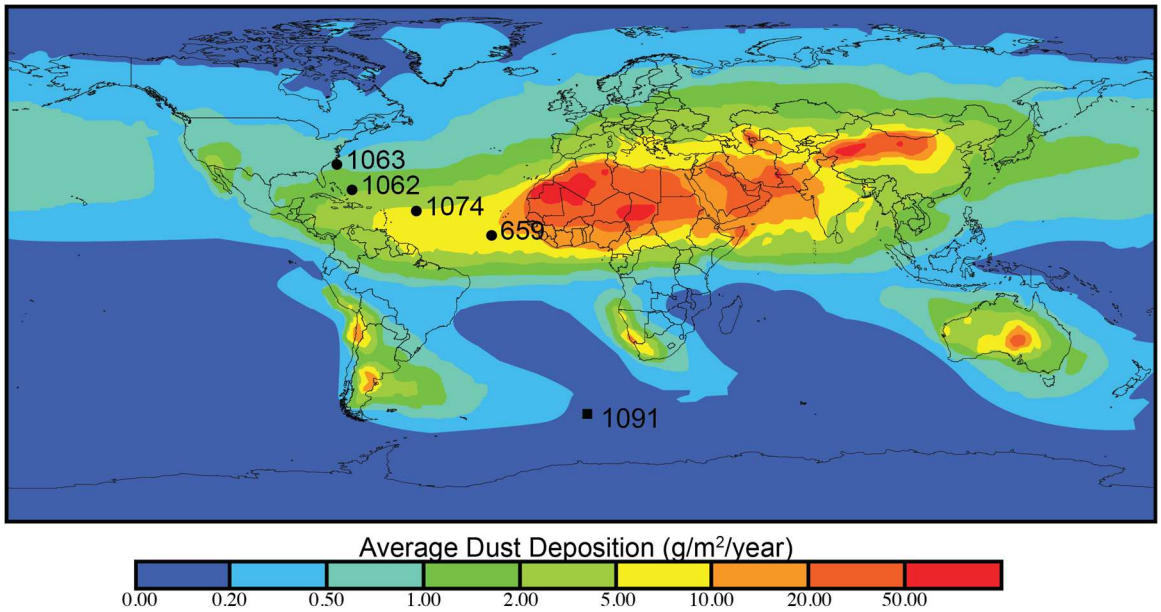

Fig. 1: Site location and distribution of dust to the oceans. (Modified from Jickells et al., 2005)

3.2 Grain Size Analysis

Grain size distributions in ocean sediments and ice cores are often used as a measure of dust delivery and related transport dynamics. Here, I used the size distributions of dust particles to investigate possible variation in highly reactive Fe content as a function of grain size [*Baker and Jickells*, 2006; *Claquin et al.*, 1999; *Ooki et al.*, 2009]. To assess possible grain size relationships, I used the traditional sieving method to separate size fractions for geochemical analysis. Grain-size distributions determined by sieving were confirmed using laser diffraction.

More specifically, a total of 109 samples were collected and dried at 80°C. Dry sieving was carried out using a tapping sieve shaker (RO-TAP) equipped with a set of stainless steel sieves (mesh sizes: 20, 43, 65 microns) for 15 min. Each fraction was weighed and recorded. The laser diffraction particle size analyzer (LDPSA) also used for

grain size analysis was a Beckman-Coulter LS 13320 located at Woods Hole Oceanographic Institution. Samples processed for LDPSA were treated with a dispersant—sodium hexametaphosphate (Calgon), $(NaPO_3)_6$—to minimize the effects of electrostatic interactions. A 60 second measurement time was adopted with analysis by the Fraunhofer diffraction method [*Eshel et al.*, 2004; *Loizeau et al.*, 1994]. Wet sieving was not performed due to the potential for altering the Fe phases present. Particle size distribution is represented graphically with cumulative distribution curve, and the cumulative distribution is obtained. The cumulative 'undersize distribution' shows a relative amount at or below a particulate grain size. To describe a particle size distribution I used the D value method [*Blott and Pye*, 2001], wherein D10, D50, and D90 represent the midpoint and range of the particle size of the sample. The particle size distributions were calculated based on sieve analysis results by creating an S-curve of cumulative mass retained in the sieve mesh and calculating the intercepts for 10%, 50% and 90% mass.

3.3 Iron Speciation and Concentrations

In past efforts to study total dust fluxes, total Fe was quantified in bulk sample digests following removal of oxides and oxyhydroxides (i.e., the best mineral candidates for Fe that was at least partially bioavailable at the time of deposition). This iron removal was part of a sediment disaggregation step, which unfortunately undermined the method's utility for approximating availabilities of bioreactive Fe. In contrast, I used a state-of-art sequential extraction procedure modified from Poulton and Canfield [*Simon W. Poulton and Canfield*, 2005] to quantify different types of Fe bound in sediments,

including Fe(III) oxides and oxyhydroxides. The quantities of oxides and oxyhydroxides provide an estimate of the potential for initial bioavailability. These phases are not all soluble in seawater, particularly long after deposition, but greater availability of Fe(III) minerals in the samples now means greater likelihood of initial, more soluble fractions in the past that subsequently recrystallized/stabilized. Because of these rapid transformations, the precise solubility/bioavailability of Fe(III) at the time of deposition is impossible to quantify. The goal here is to go beyond past efforts, however, by emphasizing Fe minerals that most likely derive, at least in part, from stabilized bioavailable precursors. In doing so, I avoid a reliance on total Fe, since much/most of that Fe would not have initially been soluble (e.g., many silicate phases). The necessary assumption is quite straightforward: greater Fe oxide and oxyhydroxide contents now might reasonably scale with a greater initial presence of labile precursor minerals.

To characterize a broader range of phases present, including minerals that might form diagenetically for initially bioreactive Fe, I extracted Fe bound in carbonates (1 M sodium acetate buffered with acetic acid to pH 4.5), reducible iron and manganese oxide and oxyhydroxide phases (50 g L^{-1} sodium dithionite buffered with acetic acid and sodium citrate to pH 4.8) and magnetite (0.2 M ammonium oxalate/0.17 M oxalic acid buffered with ammonium hydroxide to pH 3.2). These extracts were analyzed by inductively coupled plasma-mass spectrometry (ICP-MS; Agilent 7500ce) using H_2 and He in the collision cell after 100-fold dilution in trace-metal grade 2% HNO_3.

Total solid-phase iron (Fe_T) and aluminum (Al) concentrations were determined on ashed samples (550 °C) using a three-step digestion method (HNO_3/HCl/HF at

140ºC). This way, the potential bioreactivity of the Fe can be expressed as a fraction of the total Fe pool. Organic and carbonate components were estimated by ashing [*Heiri et al.*, 2001] and loss of ignitions was determined before the digestion. Final concentrations were determined on an Agilent 7500ce ICP-MS with100-fold dilution in trace-metal grade 2% HNO_3. Reference standards SDO-1 (Devonian Ohio Shale) and SCO-1 (Cody Shale) were digested and analyzed in parallel with the sample extractions and yielded errors of less than <4% and <6% for total Fe and Al, respectively.

3.4 Total Inorganic and Organic Carbon Concentrations (TIC, TOC)

Sedimentary total carbon (TC) was analyzed by combustion using an Eltra CS analyzer. Total inorganic carbon (TIC) was analyzed by acidification of a split of the same sample. The total organic carbon (TOC) content was calculated as the difference between TC and TIC.

3.5 Age Model

The age models were adjusted by graphic correlation based on shipboard micropaleontology, paleomagnetic measurements, $CaCO_3$ records and oxygen isotope chemostratigraphy ($\delta^{18}O$) for sites 1062 (Table 1) [*Franz and Tiedemann*, 2002; *Gruetzner et al.*, 2002], 1063 (Table 2 supplement) [*Channell et al.*, 2012; *Gruetzner et al.*, 2002], 659 (Table 3) [*S J Gibbs et al.*, 2005; *Haug and Tiedemann*, 1998; *Tiedemann et al.*, 1994] and 1091 (Table 4)[*Grigorov et al.*, 2002; *Kemp et al.*, 2010; *Schulz et al.*, 1998]. No exact correlation of age was established for the site 1074 due to lack of nannofossil data, isotope-based models and paleomagnetic records.

4. Results

4.1 Grain Size Distribution

Analyses of particle size distribution (PSD) by sediment sieving allowed me to isolate the dust-dominated fraction. The results show a similar retained percentage for each of the sieves with D_{50} = 43 to 57µm. (Fig. 2, Table 5). There was a loss of only1.8% during dry sieving based on comparison of the initial bulk weight and the summed size fractions following sieving. Small samples were not sieved and are not plotted.

To determine the accuracy and precision of the applied methodology, laser diffraction (LD) was performed. I compared the main parameters obtained from the two methods, and the data agree within an 11% margin of error.

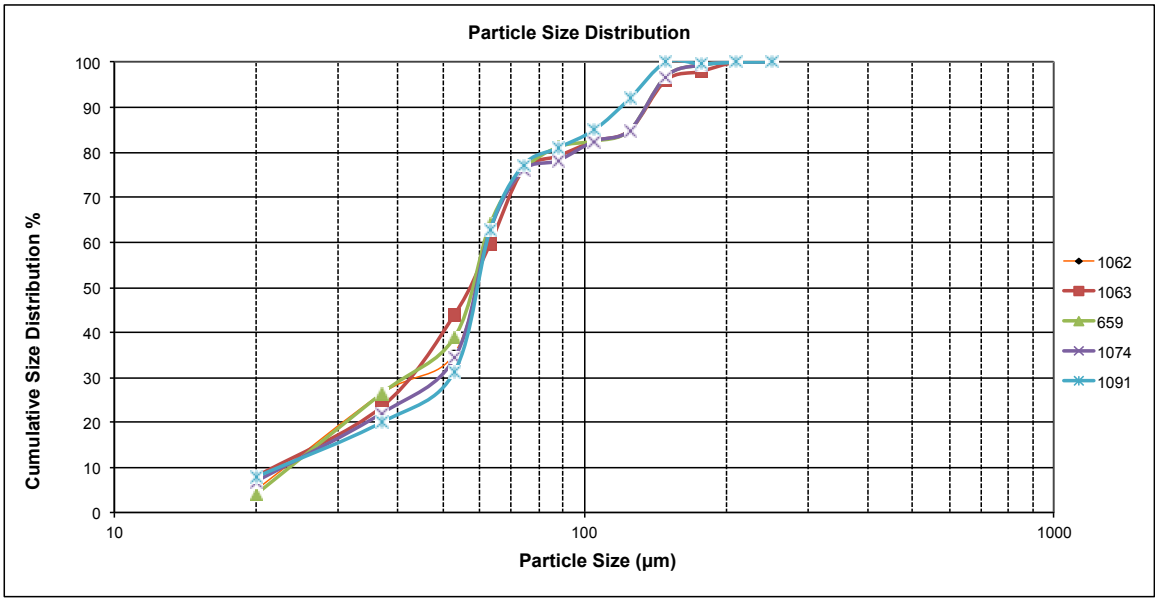

Fig. 2: Particle size distribution for all the sites.

4.2 Iron and Carbon Data

The depth profiles for TOC content are very similar for all five sites ranging from 0 to 0.7wt% (Fig. 3,4,5,6,7). These low values have important implications for the likelihood of secondary iron remobilization following burial (see discussion below). No systematic trend is found in any of these down-core distributions. Iron concentrations are presented as total Fe (Fe_T) and highly reactive Fe (Fe_{HR}), which is the sum of Fe bound in carbonates, oxides/oxyhydroxides and magnetite. Pyrite Fe is not included because concentrations are negligible as confirmed by analysis via the chromium reduction method [*Canfield et al.*, 1986] for a representative set of samples. In all cases, the Fe_{HR} fraction is dominated by the dithionite (oxide/oxyhydroxide) step (details follow).

4.2.1 Site 1091 (47.5°S, 5.5°E)

Located in the Southern Atlantic Ocean, on the western flank of the Meteor Rise (4363 m water depth), the Patagonia region is the main source of dust. Analyzed core depths range from ~0.23 to17.5 meters below seafloor (mbsf) and span in age from ~ 2.3 to 193.4 thousand years (kyr) (Table 1 supplement). Fe_T is variable, from 1.06 wt% to 2.80 wt% in the grain size fraction > 0.65 μm, from 1.48 wt% to 2.86 wt% for the fraction between 65 μm and 43 μm and 1.25 wt% to 3.13 wt% for the fraction smaller than 43 μm. Fe_{HR} is also variable, from 0.11 wt% to 0.37 wt% in the > 0.65 μm fraction, from 0.05 wt% to 0.31 wt% for the fraction < 65 μm and > 43 μm, and 0.06 wt% to 0.19 wt% for grains < 43 μm. Fe_{HR}/Fe_T ratios have average values of 0.07, and average Fe_T/Al is 0.72 (Fig. 3, Table 6a-c).

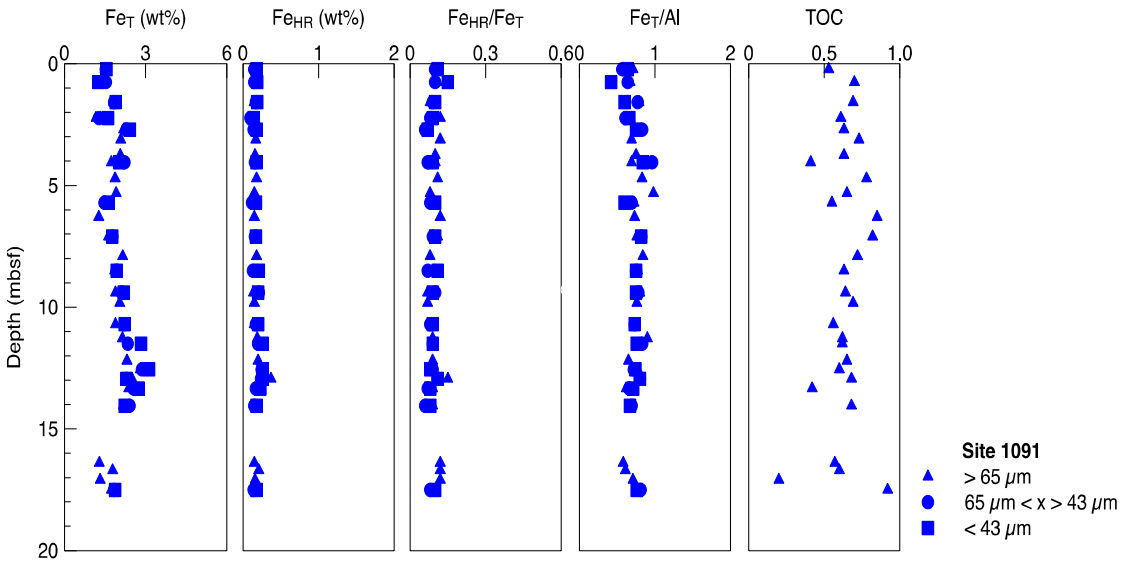

Fig. 3: Site 1091 data analysis.

4.2.2 Site 1062 (28°N, 74°W)

Located in Blake-Bahama Outer Ridge, Northern Atlantic Ocean (4763m water depth), this is a distal site relative to the Sahara region, which is nonetheless the main source of dust to this region. Analyzed core depths range from ~0.1 to 19.9 mbsf and span in age from ~15.5 to 134.4 kyr (Table 2). Fe_T is variable, from 2.21 wt% to 4.14 wt% in the grain size fractions >0.65 μm, from 2.32 wt% to 4.25 wt% for fractions between 65 μm and 43 μm, and 1.75 wt% to 4.47 wt% for fraction smaller than 43 μm. Fe_{HR} is also variable, from 0.10 wt% to 0.32 wt% in the size fraction > 0.65 μm, from 0.11 wt% to 0.36 wt% for the fraction < 65 μm and > 43 μm, and 0.14 wt% to 0.39 wt% for samples grains <43 μm. Fe_{HR}/Fe_T ratios have average values of 0.06, and average Fe_T/Al is 0.61 (Fig. 4, table 7a-c).

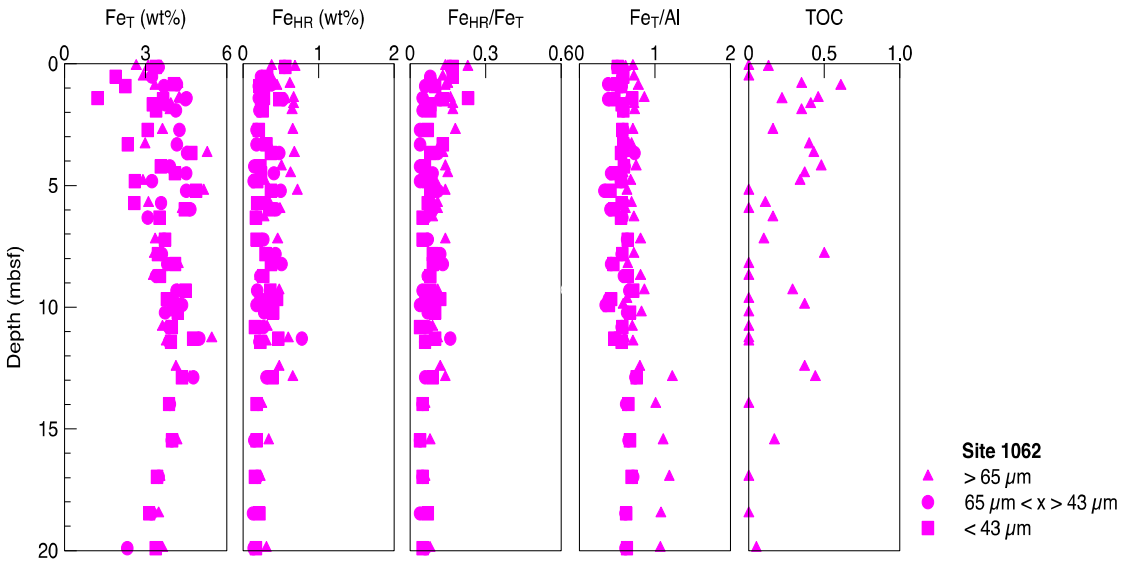

Fig.4: Site 1062 data analysis.

4.2.3 Site 1063 (33°N, 57°W)

Located in Bermuda Rise, Northern Atlantic Ocean (4583m water depth), this is also a distal site relative to the Sahara source region. Analyzed core depths range from ~0.07 to 5.04 mbsf and span in age from ~6.2 to 22.4 kyr (Table 3). Fe_T is variable, from 3.40 wt% to 5.76 wt% in the grain size fraction > 0.65 μm, from 5.58 wt% to 8.83 wt% for the fraction between 65 μm and 43 μm, and 5.19 wt% to 8.01 wt% for fractions smaller than 43 μm. Fe_{HR} is also variable, from 0.49 wt% to 1.26 wt% in the samples >0.65 μm, from 0.70 wt% to 1.41 wt% for the fraction < 65 μm and > 43 μm, and 0.61 wt% to 1.55 wt% for grains smaller than 43 μm. Fe_{HR}/ Fe_T ratios have average values of 0.21, and average Fe_T /Al is 0.57 (Fig.5, table 8a-c supplement).

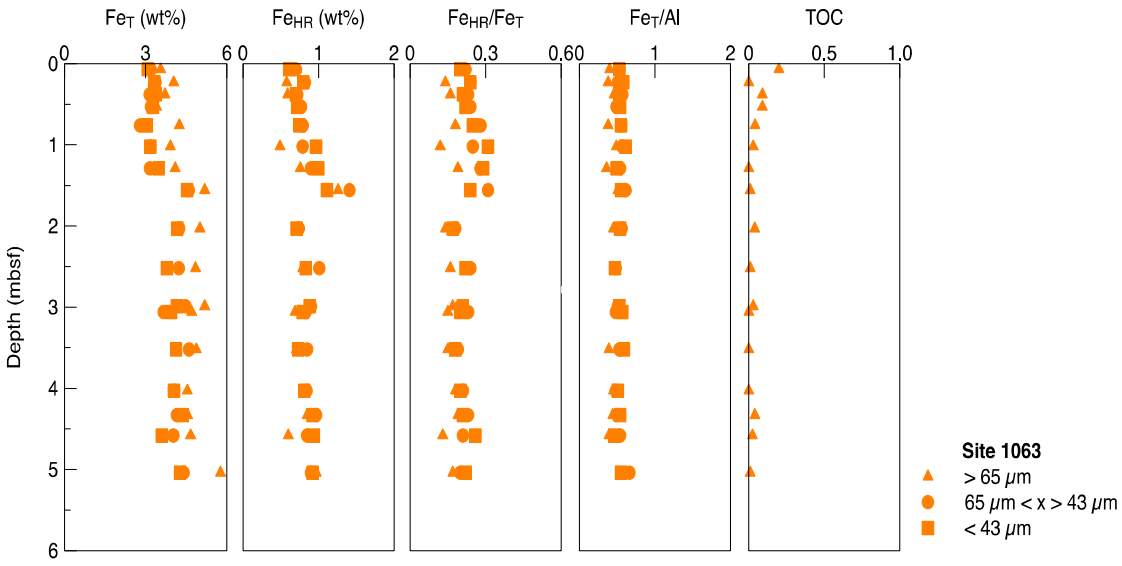

Fig. 5: Site 1063 data analysis.

4.2.4 Site 659 (18°N, 21°W)

Located on top of the Cape Verde Ridge, Northern Atlantic Ocean (3081 m water depth) is proximal site to the Sahara dust source. It has high sedimentation rate of up to 29g m^{-2} yr^{-1} over last 0.73 Ma. The analyzed core depths range from ~ 0.67 to 10.84 mbsf and in age from ~10.2 – 339 kyr (Table 4). Fe_T is variable, from 0.61 wt% to 2.64 wt% in the grain size fraction> 0.65 μm, from 0.38 wt% to 2.38 wt% for the fraction between 65 μm and 43, and 0.97 wt% to 2.38 wt% for fraction smaller than 45 μm. Fe_{HR} is also variable, from 0.24 wt% to 0.7 6wt% in the >0.65 μm fraction, from 0.20 wt% to 0.80 wt% for the fraction < 65 μm and > 43 μm, and 0.20 wt% to 0.86 wt% for grains smaller than 43 μm. Fe_{HR}/Fe_T ratios have average values of 0.27, and average Fe/Al is 0.48 (Fig. 6, table 9a-c).

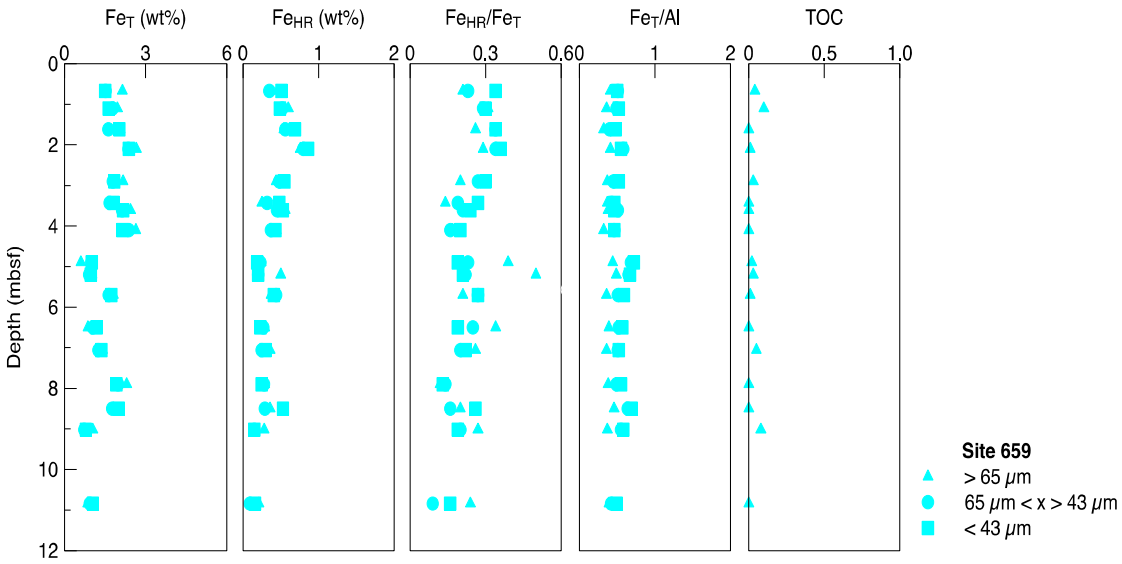

Fig. 6: Site 659 data analysis.

4.2.5 Site 1074 (22.5°N, 46.6°W)

This site is located in the North Pond area, Northern Atlantic Ocean (4445m water depth) proximal to the Sahara source region. Analyzed core depth range from ~0.05 to 1.0 mbsf. Age was not demined. Fe_T is variable, from 1.26 wt% to 4.38 wt% in the grain size fraction > 0.65 µm, from 1.29 wt% to 3.49 wt% for the fraction between 65 µm and 43 µm, and 1.20 wt% to 3.32 wt% for the fraction smaller than 45 µm. Fe_{HR} is also variable, from 0.52 wt% to 1.36 wt% in fractions > 0.65 µm, from 0.55 wt% to 1.18 wt% for the fraction < 65 µm and > 43 µm, and 0.42 wt% to 1.50 wt% for grains smaller than 43 µm. Fe_{HR}/Fe_T ratios have average values of 0.39, and average Fe/Al is 0.65 (Fig.7,table 10a-c).

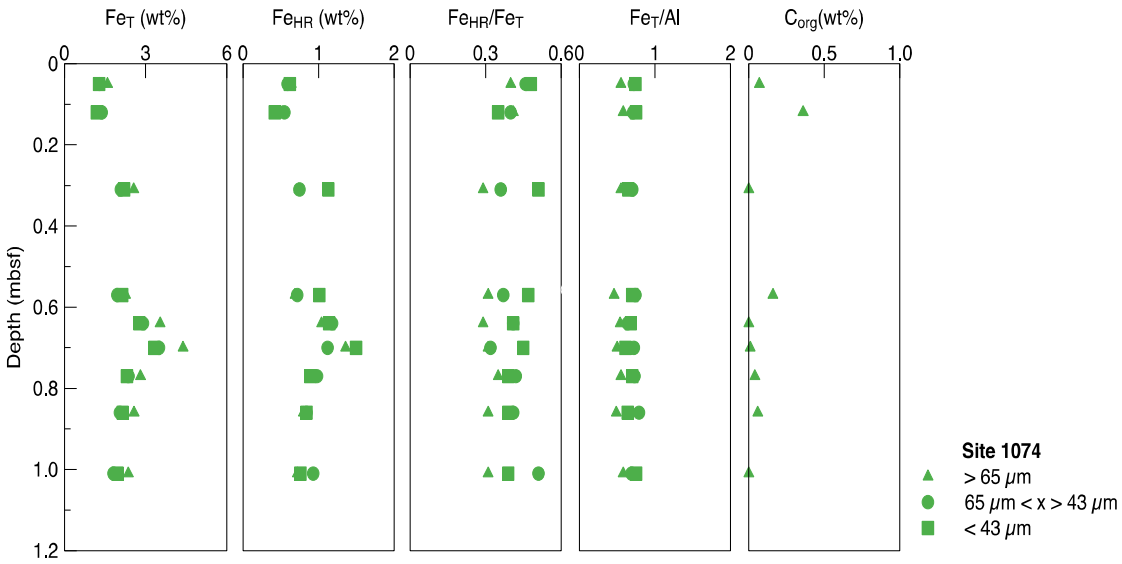

Fig. 7: Site 1074 data analysis.

5. Discussion

5.1 Estimates of bioreactive Fe

The definition of highly reactive iron (Fe_{HR}), based on the extraction scheme employed here and historical use of the term, refers to Fe minerals that are reactive toward biological and abiological reduction under anoxic conditions on short diagenetic time scales, including those phases reactive with hydrogen sulfide over the same periods [*Robert Raiswell and Canfield*, 1998]. Again, these mineral phases consist of (1) carbonate-associated Fe, (2) amorphous and crystalline Fe oxides and oxyhydroxides and (3) magnetite Fe [*Simon W. Poulton and Canfield*, 2005]. The sum of these is referred to as highly reactive Fe (Fe_{HR}) in this study. Again, pyrite contents are negligible in these samples. I normalized Fe_{HR} against Fe_T to identify possible enhancements (or deficiencies) in the reactivity relative to the total Fe pool. Similar trends can be observed for Fe_T by normalizing to Al [*Lyons and Severmann*, 2006].

$$Fe_{HR} = Fe_{cab} + Fe_{ox} + Fe_{mag} + Fe_{py}$$

$$Fe_{HR} = Fe_{cab} + Fe_{ox} + Fe_{mag}$$

More specifically, this approach highlights enrichments and depletions relative to baseline values across time and space. In addition, the ratios are insensitive to the potential artifacts of dilution (e.g., by carbonate or biogenic silica) that can lead to ambiguous or spurious interpretations of absolute concentrations. For comparison, Fe_{HR}/Fe_T ratios average 0.22 for coastal oxic to suboxic muds from diverse modern marine settings, with an upper limit of 0.38 [*Lyons and Severmann*, 2006; *Robert Raiswell and Canfield*, 1998; *R. Raiswell et al.*, 2001]. Fe_T/Al ratios for oxically deposited ancient shales of varying ages average 0.53 ± 0.11 [*R. Raiswell et al.*, 2008], which agrees well with the value for average continental crust and modern oxic muds [*Lyons and Severmann*, 2006; *S R Taylor and McLennan*, 1995].

As mentioned above, the majority of the Fe_{HR} in my samples is present now in oxide and oxyhydroxide phases. These provide the best remaining window to past potential for bioavailability because they are the minerals that most readily convert to soluble, bioreactive phases during atmospheric processing. Furthermore, they capture any secondary products formed during stabilization of those residual soluble phases, assuming incomplete dissolution, and could in theory contain phases soluble now. These are the mineral species also most vulnerable to microbial reduction under anoxic conditions. We also include carbonate-bound Fe in our calculation of Fe_{HR}, although a very minor component, because it typically forms during diagenesis through reduction of oxide/oxyhydroxide phases. We include magnetite for the same reason, although it occurs

is significant amounts in our samples and could include insoluble detrital inputs.

5.2 Fe_{HR} /Fe_T by Grain Size

Aeolian dust transported through the atmosphere carries iron-rich minerals that play an important role as marine micronutrients when delivered to the open ocean. These dust deposits are distinguished by their abundances of particles with diameters smaller than 63μm, which are transported by atmospheric suspension, although larger particles are often included. The chemical properties of dust provide information about the processes of formation and removal that are often size-dependent [*Hand et al.*, 2004; *Luo et al.*, 2005]. Iron dissolution experiments have shown enrichment of species in smaller size fractions of dust with higher iron solubility [*Baker and Jickells*, 2006; *Ooki et al.*, 2009].

Surprisingly, I found no clear differences in the Fe_{HR}/Fe_T properties of the sediment as a function of grain size, suggesting that each of my size fractions is dominated by dust derived from the same source—and with similar histories of transport and atmospheric processing (Fig. 8, Table 6-10 supplement). Consequently, the data are independent of relative surface area-to-volume relationships and thus relative grain area available for oxide coating and photochemical exposure, for example. These results are in contrast to previous work focused on dust collected in traps rather than within marine sediments. For example, recent observations in Saharan dust source regions show minor effects on iron solubility as a function particle size [*Z B Shi et al.*, 2011].

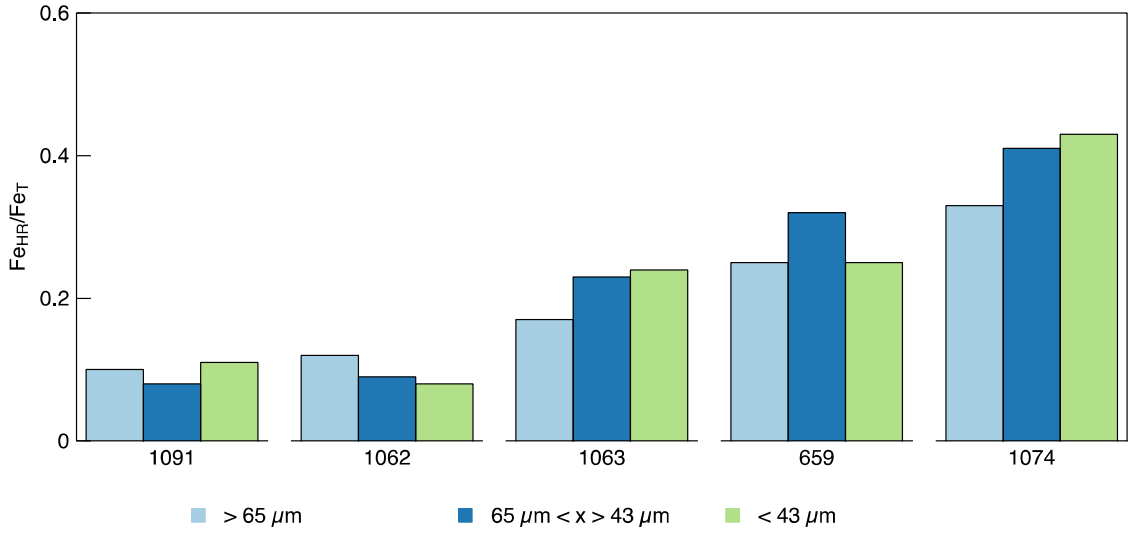

Fig. 8: Fe_{HR}/Fe_T properties of the sediment as a function of grain size.

There are large unknowns associated with estimates of bioavailable iron deposition based on grain size and mineral composition and their relationships with source region because of possible sorting during transport. However, the predominance of small particles is consistent with long-range transport. Larger particles (>~63 μm), on the other hand, move by saltation close to the ground surface, and these grains can break apart into smaller particles [*Zender et al.*, 2003]. The efficiency of incorporation and transport of aeolian dust into the atmosphere depends on friction velocity and wind speeds [*Andersen et al.*, 1998], and particle size tells us about the transport and deposition patterns because the size controls the lifetime of the aerosols in the atmosphere. There are limited data available for dust and the associated distribution of iron, and modeling has been used to fill that gap [*N M Mahowald et al.*, 2005; *J. Keith Moore et al.*, 2001].

Today, however, we have several high-quality data sources, such as satellite,

ground-based and aircraft studies that allow atmospheric modeling. The data include total iron concentrations in the aerosols and estimates of the effects of Fe inputs on primary production in the oceans[*Andersen et al.*, 1998; *Erickson et al.*, 2003; *Gao et al.*, 2001; *N M Mahowald et al.*, 2005; *J. K. Moore and Braucher*, 2008]. The available data are nonetheless still limited, particularly as related to time series relationships and specifics about the processes of entrainment, transport and deposition[*Andersen et al.*, 1998; *R Raiswell et al.*, 1994; *Reid et al.*, 2003]. Here, I interpret my data with caution, emphasizing only first-order empirical relationships, because the mechanistic details of transport, dry versus wet deposition and associated chemical effects and their impacts on iron are not well known.

5.3 Glacial-Interglacial Patterns

Dust deposition patterns are one of the most significant glacial-interglacial changes observed as potentially related to climate, CO_2 levels and carbon cycling [*Broecker*, 1982; *Harrison et al.*, 2001]. Dust deposition increases during glacial periods due to several factors. First, wind intensities increase during glacial times, allowing more dust removal and transport to the open oceans. Second, during glacial periods, cold and dry conditions reduce the rate of chemical weathering [*Andersen et al.*, 1998] but intensify physical weathering [*A Taylor and Blum*, 1995] and expose sediments on continental shelves due to low sea levels [*Andersen et al.*, 1998; *M T Gibbs and Kump*, 1994]. The net result is an overall increase of dust supply [*Farrera et al.*, 1999; *Jolly and Haxeltine*, 1997]. Lastly, dust remains in the atmosphere for longer periods as a result of reduced intensity of hydrological cycle [*Peterson et al.*, 2000].

Motivated by these previous studies, I studied the bioavailable fraction of iron deposited in the ocean over glacial-interglacial time scales. My results show no apparent glacial-interglacial variation in Fe_{HR}/Fe_T ratios for the four main sites (site 1074 is not included in this analysis due to lack of age model) (Fig. 9, table 1-4). Importantly, the lack of glacial-interglacial variation appears to be primary rather than reflecting diagenic processes for the follow reasons. Fe_T/Al ratios of 0.6 are very similar to continental crustal average (~0.5) [*A Taylor and Blum*, 1995; *S R Taylor and McLennan*, 1995] and are relatively uniform over the studied interval. There is no enrichment of iron through the sections, including the surface-most intervals where remobilized Fe commonly concentrates due to oxidation. During digenesis iron can also migrate toward organic-rich layers [*Berner*, 1969], where local pyrite enrichments can occur, or away from such layers when bacterial iron reduction dominates rather than sulfate reduction. However, I observed no such enrichments, or depletions, likely because TOC content is consistently low (0 to 0.7 wt%, mostly at or below 0.1 wt.%). Furthermore, total iron (Fe_T) ranges from 2-5.7 wt%, within the continental crust average of 4. It is also important to reminder that reader that my data speak to relative temporal Fe reactivity but not total delivery of Fe_{HR}, because the dust fluxes were likely higher during glacial intervals.

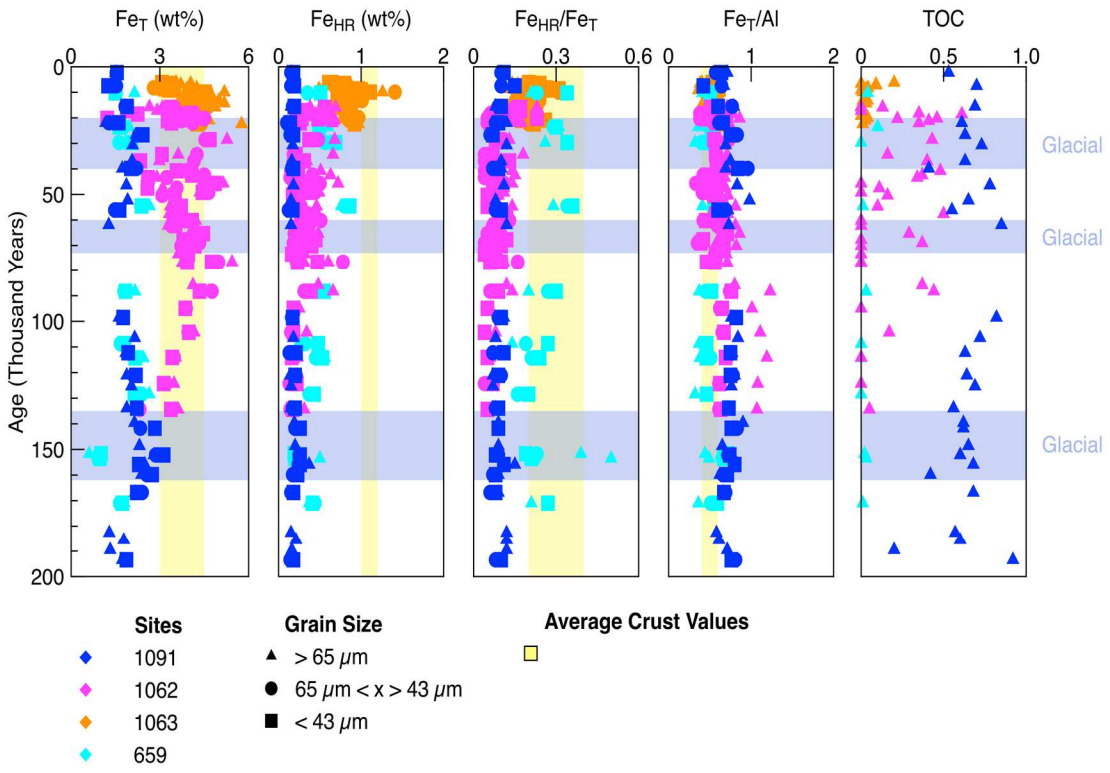

Fig. 9: Glacial-Interglacial analysis for four sites 1091, 1062, 1062 and 659.

Iron oxides and oxyhydroxides are composed of more than 50% iron, and they are often considered to be the main suppliers of dissolved iron from aeolian dust particles [*Fan et al.*, 2006], particularly when their solubilities are enhanced during atmospheric processing. Consistent with these assertions, my analyses show that Fe_{HR} is dominated by oxide phases uniformly through the cores (Fig. 10a, Table 12 supplement). More specifically, all five sites are dominated by iron extracted by dithionite—mainly iron oxy(hydr)oxides (ferrihydrite, goethite, lepidocrocite and hematite)[*Raiswell*, 2006] (Fig.10a,10b). This extraction step bears only a small contribution from iron-bearing silicates and magnetite, which could reflect a combination of diagenetic formation from more soluble Fe [*McCabe et al.*, 1983] and aeolian transport.

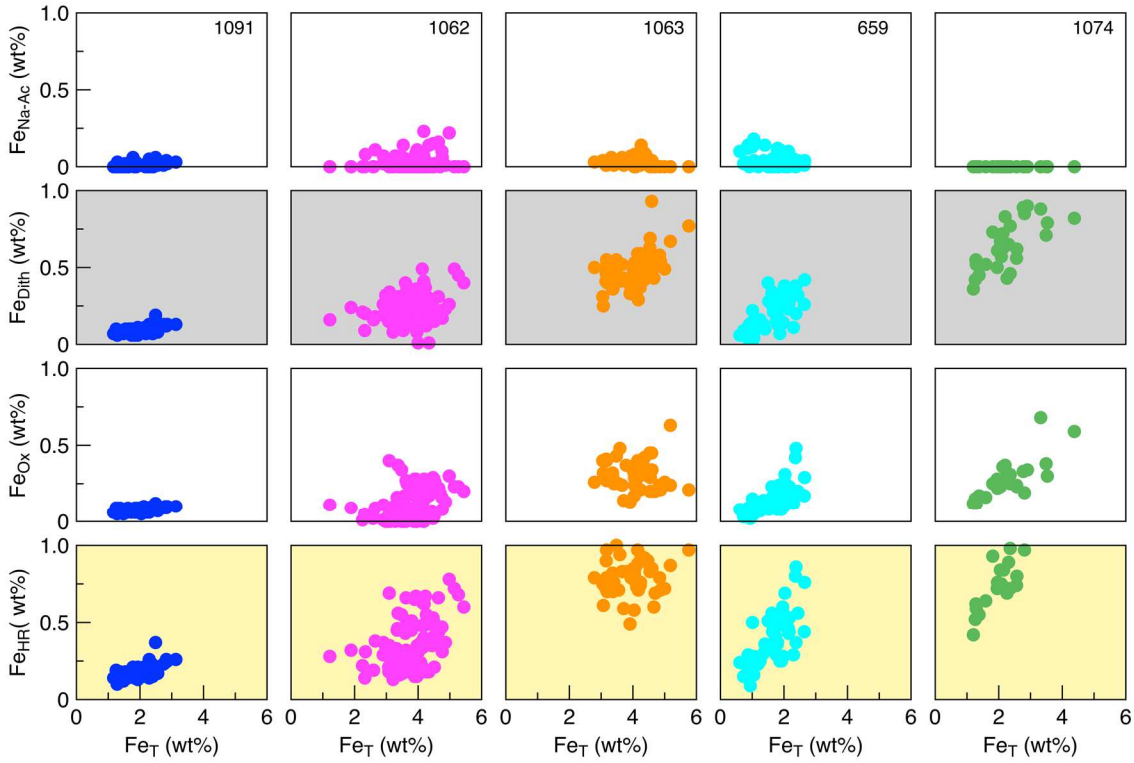

Fig. 10a: Fe_{HR} are dominated as oxide phases. Sodium acetate extracts for carbonate dissolution (siderite and ankerite). Dithionite selects reducible oxides (goethite, hematite, ferrihydrite and lepidocrocite). Oxalate extracts magnetite.

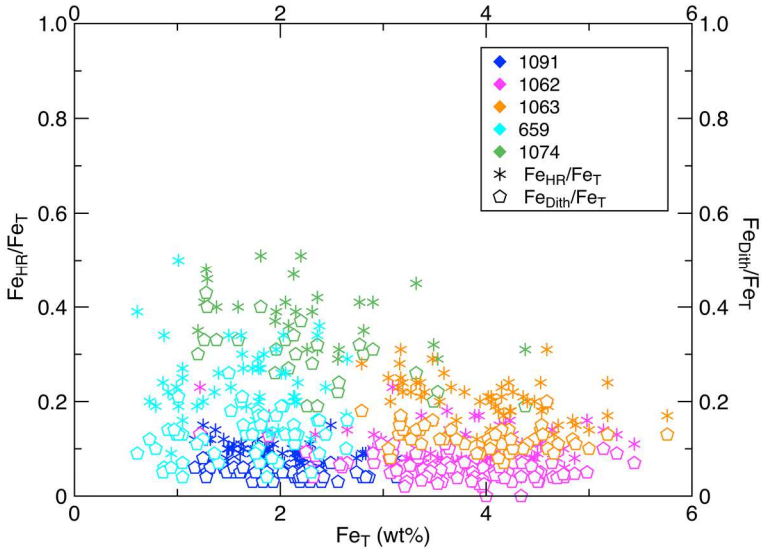

Figure 10b: The distribution of Fe_{HR}/Fe_T and Fe_{Dith}/Fe_T .

Iron solubility in marine systems is linked to complexation with prokaryotic-released organic matter (OM) such as siderophores, polycarboxylate ligands [*Barbeau*, 2006; *Pokrovsky and Schott*, 2002] and saccharides [*Hassler et al.*, 2011]. In this light, the low TOC (mostly at/or below 0.1%) is consistent with my previous assertion that Fe during diagenetic mobilization from oxides and oxyhydroxides was minor.

Wind-blown dust with Fe_{HR} is originally deposited into a microlayer at the sea surface where dissolved and colloidal organic matter (OM) are abundant and can control, along with particulate OM, the cycling of many trace elements [*Pokrovsky and Schott*, 2002]. Dust residence times in the microlayer are about 1-15 hours [*Chester et al.*, 1972] and can facilitate aqueous Fe-binding with organic ligands and/or as nanoparticulate aggregates, which can then sink [*Hunter and Boyd*, 2007]. In modern coastal marine systems, continentally derived sediments deposited under oxic bottom waters have Fe_{HR}/Fe_T ratio <0.38 and average 0.2 [*Lyons and Severmann*, 2006; *Robert Raiswell and Canfield*, 1998]. The studied sites have Fe_{HR}/Fe_T ratios 0.1-0.39 (Figure 3-7). Overall, Fe_{HR}/Fe_T values from the five IODP sites are consistent with a continental dust source, but with the low values likely reflecting selective loss of reactive (solubilized) Fe.

5.4 Fe_{HR} / Fe_T Spatial Trend

Iron linked to dust is transported downwind in the troposphere for long distances [*Prospero*, 1999; *Talbot et al.*, 1986] as well as by vertical mixing through dry or moist convection [*N Mahowald et al.*, 1999; *Rasch et al.*, 2000]. Dust removal occurs by dry and wet deposition, and those processes are dependent on aerosol particle size [*Duce and Tindale*, 1991; *Jickells et al.*, 2005]. Wet deposition occurs with removal of dust during

precipitation, where it is entrained into the water drops within or below the cloud. Dry deposition is based on gravitational settling, during which larger particles are removed as a function of their density and size. In both cases, removal includes possible altered phases produced by cloud processing. Iron solubility increases with cloud processing and solar radiation [*Luo et al.*, 2005; *Z Shi et al.*, 2012; *Spokes et al.*, 1994]. Furthermore, wet deposition can occur in solutions that may vary in pH from 4-8, which can further impact Fe solubility. Lifetimes of iron-bearing aerosols in the atmosphere are estimated to be between days (for large particles >2μm) to weeks for smaller particles [*Luo et al.*, 2005; *N Mahowald et al.*, 1999].

Atmospheric processing changes the solubility of iron as it moves from the source regions toward deposition in the oceans [*Journet et al.*, 2008; *N Mahowald et al.*, 2008; *Rasch et al.*, 2000] through process such as photochemical reactions, organic complexation and cloud processing [*Chen and Siefert*, 2004; *Desboeufs et al.*, 2001; *Hand et al.*, 2004; *Jimenez et al.*, 2009]. Atmospheric chemical processing in the clouds occurs due to increased acidity that can dissolve Fe-bearing mineral phases—oxides and oxyhydroxides in particular[*Kieber et al.*, 2001]. In the atmosphere, dust particles interact with atmospheric gases and moisture. More specifically, nitric (HNO_3) and sulfuric (H_2SO_4) acid produced in the clouds reacts with ammonia (NH_3) and ozone (O_3), resulting in a reactive mixture [*Brimblecombe*, 1996]. The variably acidic conditions of cloud moisture [*Z Shi et al.*, 2009] can cause differential dissolution of dust minerals and thus alter the properties of the iron minerals as more labile forms are reprecipitated [*Mackie et al.*, 2005]. Furthermore, iron in dust can experience multiple exposures to

moisture if not precipitated out [*Pruppacher et al.*, 1998].

Photochemical processing in the atmosphere reduces Fe(III) to more soluble Fe(II) [*Hand et al.*, 2004; *Zhu et al.*, 1997]. As a consequence, dust from distal sites might experience higher degrees of atmospheric processing that should enhance reactivity/solubility. Furthermore, atmospheric processing can produce ferrihydrite (bioavailable Fe) by changing chemical conditions in the water around mineral dust since in the atmosphere dust particles can undergo acid processes with nitrate and sulfate present [*Hand et al.*, 2004; *Z Shi et al.*, 2012]. Importantly, because of these atmospheric processes, models predict small Fe solubility and large dust deposition near the sources and large Fe solubility corresponding to smaller total dust deposition distant from source regions [*Fan et al.*, 2006; *Hand et al.*, 2004]. My data support this significant prediction.

My analyses show proximal sites (659 and 1074) with Fe_{HR}/Fe_T ratios falling at the high end of the total observed range and for marginal oxic marine sediments 0.33 (Fig. 12), and distal areas (1091,1062 and 1063) have appreciably lower Fe_{HR}/Fe_T ratios, with an average of 0.12. This trend could reflect enhanced reactivity (solubility) at the distal sites (i.e., through greater atmospheric transport/ processing) in combination with subsequent loss of that reactive iron in the water column—with important implications for the spatial gradients of primary production stimulated by dust delivery.

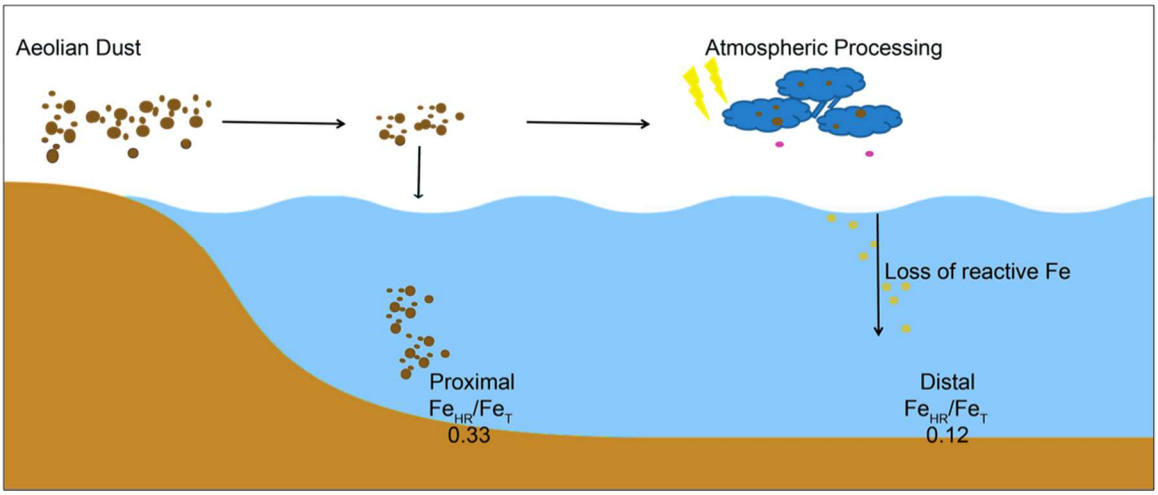

Fig. 11: Fe_{HR}/Fe_T by distance form the desert source region. Proximal sites (659 and 1074) have average Fe_{HR}/Fe_T 0.33 and the distal sites have Fe_{HR}/Fe_T average 0.12.

Iron supply models assume that atmospheric chemical processes increase the solubility (bioavailability) of iron during dust transport. The reactions of ferric iron in oxides with organic species such as oxalate or by photochemical processes increases Fe solubility by a factor of ten upon irradiation [*Siffert and Sulzberger*, 1991]. As a result, we predict less soluble Fe delivery to areas close to major dust sources and more bioavailable iron to areas far removed from the source with loss of reactive iron in the water column, which agrees with our results. In other words, smaller delivery of dust with greater Fe reactivity at greater distance from the source could shift the locus of dust-facilitated primary production away from the source region. However, the solubility of aeolian dust calls for more detailed study to distinguish the relationships among dust mineralogy, atmospheric processing and iron solubility [*N M Mahowald et al.*, 2005].

6. Conclusion

Iron is an essential micronutrient for ocean biota, and its absence has been linked to high-nutrient low-chlorophyll regions, as well as to changes in the concentration of carbon dioxide on glacial-interglacial timescales [*Martin*, 1990; *Watson et al.*, 2000]. At glacial times dust fluxes increases, corresponding to decreases in atmospheric CO_2 concentrations of about 80 p.p.m. [*Petit et al.*, 1999]. In this study, I analyzed aeolian dust, a main source of iron to the open ocean [*Fung et al.*, 2000], in five deep-sea sediment cores and observed invariant glacial-interglacial Fe_{HR}/Fe_T. The ratios were independent of grain size. In this light, glacial-interglacial differences in iron fertilization are best ascribed to temporal variance in total dust delivery.

I did, in contrast, observe a decreasing Fe_{HR}/Fe_T trend with greater distance from the source region. This pattern is opposite to what would be predicted with decreasing dust grain size and heavy mineral (silicate) content with increasing transport distance and associated physical sorting. This result implies that iron solubility is affected by atmospheric processing that increases iron reactivity during long-range transport—leading to subsequent loss of significant amounts of soluble Fe in the water column. If widely relevant, my results suggest that dust-driven primary production might be greatest far from the source region, which could help explain spatial patterns of biological activity in the modern and ancient ocean. This exciting result suggests that further similar studies are warranted to quantity the global role of dust and atmospheric processing in influencing iron biogeochemistry and its significance in global climate change.

Tables

Table 1: Age model site 1091

Lab Sample Name	Depth (mbsf)	Depth (mcd)	Age (ka)
1091-1	0.23	0.23	2.26
1091-2	0.76	0.76	7.47
1091-3	1.58	1.58	15.53
1091-4	2.23	2.23	21.92
1091-5	2.71	2.71	26.64
1091-6	3.12	3.12	30.67
1091-7	3.75	3.75	36.86
1091-8	4.05	4.05	39.81
1091-9	4.72	4.72	46.39
1091-10	5.32	5.32	52.29
1091-11	5.71	5.71	56.12
1091-12	6.3	6.3	61.92
1091-13	7.1	10.02	98.49
1091-14	7.91	10.83	106.45
1091-15	8.5	11.42	112.25
1091-16	9.4	12.32	121.09
1091-17	9.83	12.75	125.32
1091-18	10.7	13.62	133.87
1091-19	11.28	14.2	139.57
1091-20	11.5	14.42	141.73
1091-21	12.2	15.12	148.61
1091-22	12.56	15.48	152.15
1091-23	12.94	15.86	155.88
1091-24	13.34	16.26	159.82
1091-25	14.05	16.97	166.79
1091-26	16.4	18.58	182.62
1091-27	16.7	18.88	185.57
1091-28	17.1	19.28	189.50
1091-29	17.5	19.68	193.43

Table 2:Age Model site 1062

Lab Sample Name	Depth (mbsf)	Depth (mcd)	Age (ka)
1062-1	0.1	0.1	15.77
1062-2	0.14	0.14	15.9
1062-3	0.53	0.53	17.19
1062-4	0.84	0.84	18.24
1062-5	0.92	0.92	18.51
1062-6	1.41	1.41	20.2
1062-7	1.46	1.46	20.37
1062-8	1.67	1.67	21.11
1062-9	1.92	1.92	22
1062-10	2.72	5.12	34.34
1062-11	3.32	5.72	36.85
1062-12	3.67	3.67	28.53
1062-13	4.22	6.62	40.73
1062-14	4.5	7	42.41
1062-15	4.82	7.22	43.39
1062-16	5.22	7.72	45.66
1062-17	5.72	8.12	47.5
1062-18	5.98	8.48	49.18
1062-19	6.32	8.72	50.32
1062-20	7.22	9.62	54.66
1062-21	7.82	10.22	57.64
1062-22	8.23	10.73	60.21
1062-23	8.72	11.12	62.21
1062-24	9.32	11.72	65.34
1062-25	9.67	12.17	67.73
1062-26	9.91	12.41	69.01
1062-27	10.22	12.62	70.15
1062-28	10.82	13.22	73.43
1062-29	11.29	13.79	76.61
1062-30	11.42	13.82	76.77
1062-31	12.46	15.38	85.76
1062-32	12.88	15.8	88.25
1062-33	13.98	16.9	94.92
1062-34	15.47	18.39	104.28
1062-35	16.97	19.89	114.09
1062-36	18.47	21.39	124.29
1062-37	19.9	22.82	134.37

Table 3:Age Model Site 1063

Lab Sample Name	Depth (mbsf)	Depth (mcd)	Age (ka)
1063-1	0.07	0.07	6.16
1063-2	0.23	0.23	6.53
1063-3	0.38	0.38	6.88
1063-4	0.53	0.53	7.23
1063-5	0.76	0.96	8.23
1063-6	1.02	1.15	8.67
1063-7	1.29	1.33	9.09
1063-8	1.56	1.69	9.92
1063-9	2.03	3.07	13.13
1063-10	2.52	3.11	13.22
1063-11	2.99	3.56	14.26
1063-12	3.06	4.07	15.45
1063-13	3.52	4.24	15.84
1063-14	4.03	5.68	19.18
1063-15	4.33	6.02	19.97
1063-16	4.58	6.43	20.93
1063-17	5.04	7.06	22.39

Table 4: Age Model site 659

Lab Sample Name	Depth (mbsf)	Depth (mcd)	Age (ka)
659-1	0.67	0.67	10.24
659-2	1.1	1.1	23.56
659-3	1.62	1.62	29.66
659-4	2.1	2.1	54.52
659-5	2.9	2.9	88.26
659-6	3.43	3.43	108.69
659-7	3.61	3.61	114.26
659-8	4.1	4.1	128.43
659-9	4.9	4.9	151.70
659-10	5.2	5.2	153.49
659-11	5.7	5.7	170.97
659-12	6.5	6.5	201.24
659-13	7.06	7.06	232.08
659-14	7.9	7.9	258.08
659-15	8.5	8.5	273.16
659-16	9.02	9.02	287.76
659-17	10.84	10.84	339.21

Table 5: Sieving grain distribution.

	Passing %				
Sieve Analysis	1062	1063	659	1074	1091
250.0	100.0	100.0	100.0	100.0	100.0
210.0	100.0	100.0	100.0	100.0	100.0
177.0	99.7	98.0	99.4	99.4	99.7
149.0	96.8	96.0	96.8	96.8	100.0
125.0	85.0	85.0	85.0	85.0	92.0
105.0	82.5	82.5	82.5	82.5	85.0
88.0	79.2	79.2	81.2	78.2	81.0
74.0	75.9	75.9	75.9	75.9	77.0
63.0	62.7	59.7	64.0	62.7	62.7
53.0	35.4	44.0	39.0	34.4	31.4
37.0	26.4	23.4	26.4	22.0	20.0
20.0	5.0	6.0	4.0	6.9	7.9

Table 6-a: Site 1091 (>0.65 µm)

	Sequential Fe Extraction				Total Digest		Ratio	
Lab Sample Name (>0.65 µm)	Sodium Acetate Fe (wt%)	Dithionite Fe (wt%)	Oxalate Fe (wt%)	FeHR (wt%)	Al Total (wt%)	Fe Total (wt%)	Fe_T/Al	Fe_{HR}/Fe_T
1091-1	0.00	0.09	0.07	0.16	2.12	1.50	0.71	0.10
1091-2	0.00	0.09	0.09	0.18	2.04	1.37	0.67	0.14
1091-3	0.00	0.07	0.08	0.15	2.30	1.82	0.79	0.08
1091-4	0.00	0.07	0.06	0.14	1.83	1.17	0.64	0.12
1091-5	0.01	0.07	0.07	0.15	2.80	2.19	0.78	0.07
1091-6	0.00	0.09	0.08	0.17	1.45	2.08	1.44	0.08
1091-7	0.00	0.09	0.06	0.16	1.54	2.06	1.34	0.08
1091-8	0.01	0.10	0.06	0.17	2.49	1.73	0.69	0.10
1091-9	0.00	0.10	0.07	0.18	1.55	1.87	1.21	0.09
1091-10	0.00	0.08	0.07	0.15	1.88	1.91	1.02	0.08
1091-11	0.00	0.08	0.07	0.15	2.06	1.49	0.72	0.10
1091-12	0.00	0.08	0.07	0.15	1.75	1.27	0.73	0.12
1091-13	0.00	0.08	0.09	0.18	2.14	1.62	0.76	0.11
1091-14	0.01	0.11	0.06	0.18	2.55	2.15	0.84	0.08
1091-15	0.01	0.09	0.09	0.19	2.40	1.85	0.77	0.10
1091-16	0.01	0.07	0.06	0.14	2.35	1.88	0.80	0.07
1091-17	0.01	0.09	0.05	0.15	2.71	2.04	0.76	0.07
1091-18	0.01	0.08	0.06	0.15	2.62	1.88	0.72	0.08
1091-19	0.01	0.09	0.08	0.19	2.37	2.14	0.90	0.09
1091-20	0.03	0.12	0.07	0.22	2.96	2.34	0.79	0.09
1091-21	0.01	0.11	0.08	0.20	3.54	2.31	0.65	0.09
1091-22	0.02	0.12	0.10	0.24	3.61	2.80	0.77	0.09
1091-23	0.06	0.19	0.12	0.37	3.14	2.49	0.79	0.15
1091-24	0.00	0.12	0.10	0.23	3.86	2.38	0.62	0.09
1091-25	0.00	0.09	0.09	0.19	3.29	2.17	0.66	0.09
1091-26	0.03	0.06	0.06	0.15	2.23	1.29	0.58	0.12
1091-27	0.06	0.07	0.07	0.21	2.91	1.78	0.61	0.12
1091-28	0.00	0.08	0.07	0.16	1.85	1.32	0.71	0.12
1091-29	0.02	0.06	0.08	0.16	2.26	1.73	0.77	0.09

Table 6-b: 1091 (65 µm < x < 43 µm)

	Sequential Fe Extraction				Total Digest		Ratio	
Lab Sample Name (65 µm<x <43 µm)	Na Acetate Fe (wt%)	Dithionite Fe (wt%)	Oxalate Fe (wt%)	Total Reactive Fe (wt%)	Al Total (wt%)	Fe Total (wt%)	Fe_T/Al	Fe_{HR}/Fe_T
1091-1	0.02	0.08	0.06	0.15	2.68	1.53	0.57	0.10
1091-2	0.00	0.08	0.07	0.15	2.39	1.53	0.64	0.10
1091-3	0.01	0.08	0.08	0.17	2.36	1.83	0.77	0.09
1091-4	0.00	0.06	0.05	0.10	2.12	1.28	0.61	0.08
1091-5	0.00	0.08	0.06	0.14	2.77	2.29	0.83	0.06
1091-6	N.S.	N.S.	N.S.	N.S.	N.S.	N.S.	N.S.	N.S.
1091-7	N.S.	N.S.	N.S.	N.S.	N.S.	N.S.	N.S.	N.S.
1091-8	0.02	0.08	0.06	0.16	2.31	2.21	0.96	0.07
1091-9	N.S.	N.S.	N.S.	N.S.	N.S.	N.S.	N.S.	N.S.
1091-10	N.S.	N.S.	N.S.	N.S.	N.S.	N.S.	N.S.	N.S.
1091-11	0.00	0.07	0.05	0.12	2.16	1.48	0.69	0.08
1091-12	N.S.	N.S.	N.S.	N.S.	N.S.	N.S.	N.S.	N.S.
1091-13	0.01	0.09	0.07	0.16	2.14	1.76	0.82	0.09
1091-14	N.S.	N.S.	N.S.	N.S.	N.S.	N.S.	N.S.	N.S.
1091-15	0.01	0.06	0.06	0.13	2.58	1.93	0.75	0.07
1091-16	0.01	0.10	0.10	0.21	2.73	2.12	0.78	0.10
1091-17	N.S.	N.S.	N.S.	N.S.	N.S.	N.S.	N.S.	N.S.
1091-18	0.01	0.08	0.08	0.17	3.04	2.22	0.73	0.08
1091-19	N.S.	N.S.	N.S.	N.S.	N.S.	N.S.	N.S.	N.S.
1091-20	0.04	0.09	0.08	0.20	2.81	2.34	0.83	0.09
1091-21	N.S.	N.S.	N.S.	N.S.	N.S.	N.S.	N.S.	N.S.
1091-22	0.02	0.13	0.10	0.25	3.98	2.86	0.72	0.09
1091-23	0.05	0.10	0.09	0.24	2.87	2.29	0.80	0.11
1091-24	0.01	0.08	0.07	0.17	3.87	2.56	0.66	0.07
1091-25	0.00	0.07	0.08	0.15	3.47	2.40	0.69	0.06
1091-26	N.S.	N.S.	N.S.	N.S.	N.S.	N.S.	N.S.	N.S.
1091-27	N.S.	N.S.	N.S.	N.S.	N.S.	N.S.	N.S.	N.S.
1091-28	N.S.	N.S.	N.S.	N.S.	N.S.	N.S.	N.S.	N.S.
1091-29	0.02	0.06	0.06	0.14	2.26	1.83	0.81	0.08

Table 6-c: Site 1091 (<43µm)

	Sequential Fe Extraction				Total Digest		Ratio	
Lab Sample Name (<43 µm)	Na Acetate Fe (wt%)	Dithionite Fe (wt%)	Oxalate Fe (wt%)	Total Reactive Fe (wt%)	Al Total (wt%)	Fe Total (wt%)	Fe_T/Al	Fe_{HR}/Fe_T
1091-1	0.01	0.09	0.07	0.18	2.42	1.55	0.64	0.11
1091-2	0.00	0.10	0.09	0.19	2.93	1.25	0.42	0.15
1091-3	0.01	0.09	0.09	0.19	3.12	1.89	0.60	0.10
1091-4	0.00	0.09	0.06	0.14	2.45	1.61	0.66	0.09
1091-5	0.00	0.10	0.08	0.18	3.25	2.42	0.75	0.07
1091-6	N.S.	N.S.	N.S.	N.S.	N.S.	N.S.	N.S.	N.S.
1091-7	N.S.	N.S.	N.S.	N.S.	N.S.	N.S.	N.S.	N.S.
1091-8	0.01	0.10	0.07	0.18	2.41	2.02	0.84	0.09
1091-9	N.S.	N.S.	N.S.	N.S.	N.S.	N.S.	N.S.	N.S.
1091-10	N.S.	N.S.	N.S.	N.S.	N.S.	N.S.	N.S.	N.S.
1091-11	0.00	0.10	0.07	0.17	2.72	1.64	0.60	0.10
1091-12	N.S.	N.S.	N.S.	N.S.	N.S.	N.S.	N.S.	N.S.
1091-13	0.01	0.10	0.07	0.17	2.14	1.76	0.82	0.10
1091-14	N.S.	N.S.	N.S.	N.S.	N.S.	N.S.	N.S.	N.S.
1091-15	0.01	0.11	0.09	0.21	2.58	1.93	0.75	0.11
1091-16	0.01	0.10	0.09	0.20	2.92	2.19	0.75	0.09
1091-17	N.S.	N.S.	N.S.	N.S.	N.S.	N.S.	N.S.	N.S.
1091-18	0.01	0.11	0.08	0.20	3.04	2.22	0.73	0.09
1091-19	N.S.	N.S.	N.S.	N.S.	N.S.	N.S.	N.S.	N.S.
1091-20	0.04	0.12	0.09	0.26	3.71	2.83	0.76	0.09
1091-21	N.S.	N.S.	N.S.	N.S.	N.S.	N.S.	N.S.	N.S.
1091-22	0.03	0.13	0.10	0.26	4.22	3.13	0.74	0.08
1091-23	0.04	0.13	0.09	0.26	2.87	2.29	0.80	0.11
1091-24	0.01	0.13	0.09	0.23	3.84	2.74	0.71	0.08
1091-25	0.00	0.09	0.09	0.18	3.30	2.22	0.67	0.08
1091-26	N.S.	N.S.	N.S.	N.S.	N.S.	N.S.	N.S.	N.S.
1091-27	N.S.	N.S.	N.S.	N.S.	N.S.	N.S.	N.S.	N.S.
1091-28	N.S.	N.S.	N.S.	N.S.	N.S.	N.S.	N.S.	N.S.
1091-29	0.03	0.09	0.07	0.18	2.44	1.87	0.76	0.10

Table 7-a: Site 1062 (>0.65 µm)

	Sequential Fe Extraction				Total Digest		Ratio	
Lab Sample Name (>0.65 µm)	Na Acetate Fe (wt%)	Dithionite Fe (wt%)	Oxalate Fe (wt%)	Total Reactive Fe (wt%)	Al Total (wt%)	Fe Total (wt%)	Fe_T/Al	Fe_{HR}/Fe_T
1062-1	0.11	0.09	0.18	0.37	3.72	2.65	0.71	0.14
1062-2	0.00	0.40	0.29	0.70	5.05	3.09	0.61	0.23
1062-3	0.07	0.11	0.19	0.37	4.02	2.91	0.72	0.13
1062-4	0.00	0.28	0.34	0.62	7.42	4.19	0.56	0.15
1062-5	0.01	0.16	0.28	0.45	4.29	3.34	0.78	0.14
1062-6	0.04	0.26	0.37	0.67	4.90	4.23	0.86	0.16
1062-7	0.00	0.25	0.30	0.55	6.25	4.26	0.68	0.13
1062-8	0.03	0.28	0.36	0.67	5.43	3.93	0.72	0.17
1062-9	0.06	0.28	0.31	0.65	5.33	3.89	0.73	0.17
1062-10	0.05	0.27	0.34	0.66	5.11	3.62	0.71	0.18
1062-11	0.02	0.00	0.32	0.34	4.34	2.98	0.69	0.12
1062-12	0.00	0.23	0.45	0.68	8.50	5.27	0.62	0.13
1062-13	0.03	0.10	0.38	0.51	4.87	3.64	0.75	0.14
1062-14	0.00	0.14	0.49	0.63	7.15	4.13	0.58	0.15
1062-15	0.02	0.01	0.26	0.30	4.29	2.90	0.68	0.10
1062-16	0.00	0.23	0.49	0.73	8.15	5.14	0.63	0.14
1062-17	0.01	0.00	0.34	0.35	4.47	3.10	0.69	0.11
1062-18	0.00	0.19	0.30	0.50	7.15	4.35	0.61	0.11
1062-19	0.03	0.00	0.25	0.28	4.22	3.06	0.72	0.09
1062-20	0.04	0.11	0.31	0.46	4.12	3.35	0.81	0.14
1062-21	0.03	0.01	0.29	0.33	4.58	3.32	0.72	0.10
1062-22	0.00	0.15	0.23	0.38	6.55	4.21	0.64	0.09
1062-23	0.07	0.00	0.15	0.21	4.07	3.28	0.81	0.07
1062-24	0.07	0.00	0.41	0.48	4.87	4.18	0.86	0.11
1062-25	0.00	0.13	0.18	0.31	6.36	4.01	0.63	0.08
1062-26	0.00	0.10	0.21	0.31	6.84	3.96	0.58	0.08
1062-27	0.11	0.00	0.24	0.35	4.82	3.97	0.82	0.09
1062-28	0.03	0.02	0.27	0.32	5.18	3.62	0.70	0.09
1062-29	0.00	0.20	0.40	0.59	9.00	5.44	0.60	0.11
1062-30	0.03	0.02	0.26	0.31	5.30	3.76	0.71	0.08
1062-31	0.05	0.08	0.35	0.48	5.18	4.12	0.80	0.12
1062-32	0.16	0.19	0.31	0.65	3.75	4.64	1.23	0.14
1062-33	0.05	0.00	0.20	0.25	3.84	3.87	1.01	0.06

1062-34	0.08	0.00	0.26	0.34	3.74	4.16	1.11	0.08
1062-35	0.01	0.00	0.22	0.23	2.96	3.53	1.19	0.06
1062-36	0.06	0.00	0.16	0.22	3.21	3.48	1.08	0.06
1062-37	0.05	0.00	0.26	0.30	3.39	3.62	1.07	0.08

Table 7-b: 1062 (65 µm < x < 43 µm)

	Sequential Fe Extraction				Total Digest		Ratio	
Lab Sample Name (65 µm<x <43 µm)	Na Acetate Fe (wt%)	Dithionite Fe (wt%)	Oxalate Fe (wt%)	Total Reactive Fe (wt%)	Al Total (wt%)	Fe Total (wt%)	Fe_T/Al	Fe_{HR}/Fe_T
1062-1	N.S.	N.S.	N.S.	N.S.	N.S.	N.S.	N.S.	N.S.
1062-2	0.00	0.34	0.21	0.56	6.94	3.48	0.50	0.16
1062-3	0.00	0.10	0.14	0.24	5.66	3.23	0.57	0.08
1062-4	0.00	0.10	0.28	0.39	10.86	4.15	0.38	0.09
1062-5	0.00	0.03	0.18	0.21	6.61	3.68	0.56	0.06
1062-6	0.02	0.04	0.15	0.22	6.55	4.51	0.69	0.05
1062-7	0.00	0.29	0.24	0.53	11.79	4.47	0.38	0.12
1062-8	0.01	0.03	0.20	0.24	6.52	3.73	0.57	0.06
1062-9	0.01	0.02	0.20	0.22	7.05	4.11	0.58	0.05
1062-10	0.03	0.03	0.12	0.18	7.29	4.25	0.58	0.04
1062-11	0.01	0.01	0.16	0.18	6.77	4.15	0.61	0.04
1062-12	0.01	0.26	0.22	0.48	1.22	0.53	0.43	0.91
1062-13	0.00	0.03	0.11	0.15	6.52	3.89	0.60	0.04
1062-14	0.00	0.25	0.15	0.41	10.71	4.50	0.42	0.09
1062-15	0.01	0.03	0.10	0.14	5.86	3.23	0.55	0.04
1062-16	0.02	0.28	0.21	0.50	13.54	4.50	0.33	0.11
1062-17	0.01	0.17	0.11	0.28	6.20	3.57	0.58	0.08
1062-18	0.02	0.22	0.20	0.44	11.40	4.65	0.41	0.09
1062-19	0.01	0.01	0.16	0.18	5.44	3.08	0.57	0.06
1062-20	0.01	0.04	0.22	0.27	5.86	3.68	0.63	0.07
1062-21	0.00	0.03	0.40	0.43	6.41	3.60	0.56	0.12
1062-22	0.00	0.25	0.26	0.51	9.00	3.80	0.42	0.13
1062-23	0.00	0.06	0.17	0.23	5.71	3.39	0.59	0.07
1062-24	0.00	0.03	0.17	0.19	6.31	4.14	0.66	0.05
1062-25	0.02	0.20	0.01	0.23	10.17	4.00	0.39	0.06
1062-26	0.00	0.17	0.01	0.18	12.30	4.34	0.35	0.04
1062-27	0.00	0.03	0.24	0.28	5.94	3.72	0.63	0.07

1062-28	0.00	0.04	0.23	0.27	6.88	3.86	0.56	0.07
1062-29	0.22	0.30	0.26	0.78	10.34	4.98	0.48	0.16
1062-30	0.00	0.03	0.19	0.22	6.83	3.87	0.57	0.06
1062-31	N.S.	N.S.	N.S.	N.S.	N.S.	N.S.	N.S.	N.S.
1062-32	0.06	0.08	0.17	0.31	6.47	4.76	0.74	0.06
1062-33	0.00	0.04	0.16	0.20	6.31	3.89	0.62	0.05
1062-34	0.01	0.06	0.08	0.15	6.04	3.96	0.65	0.04
1062-35	0.00	0.04	0.15	0.19	4.92	3.48	0.71	0.05
1062-36	0.00	0.05	0.08	0.13	5.23	3.21	0.61	0.04
1062-37	0.00	0.05	0.09	0.14	3.81	2.32	0.61	0.06

Table 7-c: Site 1062 (<43µm)

	Sequential Fe Extraction				Total Digest		Ratio	
Lab Sample Name (<43 µm)	Na Acetate Fe (wt%)	Dithionite Fe (wt%)	Oxalate Fe (wt%)	Total Reactive Fe (wt%)	Al Total (wt%)	Fe Total (wt%)	Fe_T/Al	Fe_{HR}/Fe_T
1062-1	N.S.	N.S.	N.S.	N.S.	N.S.	N.S.	N.S.	N.S.
1062-2	0.00	0.37	0.19	0.56	6.61	3.37	0.51	0.17
1062-3	0.00	0.09	0.24	0.32	3.24	1.89	0.58	0.17
1062-4	0.00	0.15	0.18	0.32	8.11	4.04	0.50	0.08
1062-5	0.00	0.01	0.21	0.22	4.08	2.25	0.55	0.10
1062-6	0.00	0.11	0.16	0.28	1.75	1.22	0.70	0.23
1062-7	0.00	0.25	0.22	0.48	7.95	3.65	0.46	0.13
1062-8	0.01	0.03	0.21	0.25	5.80	3.26	0.56	0.08
1062-9	0.02	0.06	0.19	0.26	5.84	3.39	0.58	0.08
1062-10	0.02	0.04	0.15	0.21	5.41	3.07	0.57	0.07
1062-11	0.08	0.03	0.20	0.31	4.06	2.34	0.58	0.13
1062-12	0.00	0.19	0.18	0.37	8.46	4.69	0.55	0.08
1062-13	0.01	0.02	0.20	0.23	6.03	3.56	0.59	0.06
1062-14	0.00	0.03	0.21	0.24	8.74	4.08	0.47	0.06
1062-15	0.00	0.03	0.16	0.19	4.74	2.60	0.55	0.07
1062-16	0.01	0.13	0.23	0.37	11.75	4.86	0.41	0.08
1062-17	0.00	0.02	0.17	0.19	4.63	2.58	0.56	0.07
1062-18	0.00	0.07	0.28	0.35	9.63	4.44	0.46	0.08
1062-19	0.00	0.04	0.13	0.17	6.43	3.51	0.55	0.05
1062-20	0.00	0.04	0.14	0.18	5.85	3.72	0.64	0.05
1062-21	0.07	0.04	0.18	0.30	6.07	3.46	0.57	0.09
1062-22	0.00	0.20	0.18	0.37	9.17	4.09	0.45	0.09

1062-23	0.14	0.04	0.09	0.27	5.51	3.53	0.64	0.08
1062-24	0.15	0.02	0.18	0.36	6.31	4.47	0.71	0.08
1062-25	0.01	0.18	0.27	0.45	9.03	3.79	0.42	0.12
1062-26	0.00	0.11	0.25	0.36	10.58	4.13	0.39	0.09
1062-27	0.23	0.01	0.16	0.40	6.27	4.18	0.67	0.10
1062-28	0.00	0.02	0.14	0.16	6.96	3.96	0.57	0.04
1062-29	0.10	0.16	0.22	0.47	10.25	4.75	0.46	0.10
1062-30	0.09	0.04	0.10	0.23	7.03	3.93	0.56	0.06
1062-31	N.S.	N.S.	N.S.	N.S.	N.S.	N.S.	N.S.	N.S.
1062-32	0.14	0.06	0.18	0.39	5.72	4.34	0.76	0.09
1062-33	0.02	0.04	0.12	0.18	5.98	3.86	0.65	0.05
1062-34	0.04	0.04	0.10	0.18	5.96	3.98	0.67	0.04
1062-35	0.01	0.02	0.14	0.16	4.96	3.42	0.69	0.05
1062-36	0.00	0.06	0.17	0.22	5.07	3.13	0.62	0.07
1062-37	0.02	0.04	0.11	0.17	5.35	3.37	0.63	0.05

Table 8-a: Site 1063 (>0.65 µm)

	Sequential Fe Extraction				Total Digest		Ratio	
Lab Sample Name (>0.65 µm)	Na Acetate Fe (wt%)	Dithionite Fe (wt%)	Oxalate Fe (wt%)	Total Reactive Fe (wt%)	Al Total (wt%)	Fe Total (wt%)	Fe_T/Al	Fe_{HR}/Fe_T
1063-1	0.03	0.44	0.25	0.71	8.79	3.55	0.40	0.20
1063-2	0.00	0.42	0.17	0.58	10.49	4.04	0.38	0.14
1063-3	0.01	0.43	0.14	0.59	7.99	3.71	0.46	0.16
1063-4	0.01	0.50	0.25	0.76	6.85	3.40	0.50	0.22
1063-5	0.03	0.52	0.21	0.76	11.20	4.24	0.38	0.18
1063-6	0.03	0.33	0.13	0.49	8.03	3.91	0.49	0.12
1063-7	0.00	0.52	0.25	0.76	11.35	4.09	0.36	0.19
1063-8	0.00	0.67	0.63	1.26	10.14	5.18	0.51	0.24
1063-9	0.00	0.49	0.26	0.72	11.00	5.00	0.45	0.14
1063-10	0.00	0.58	0.24	0.79	10.16	4.84	0.48	0.16
1063-11	0.00	0.67	0.24	0.87	9.97	5.18	0.52	0.17
1063-12	0.00	0.54	0.20	0.69	9.33	4.70	0.50	0.15
1063-13	0.00	0.54	0.21	0.71	12.53	4.87	0.39	0.15
1063-14	0.00	0.69	0.20	0.83	10.16	4.54	0.45	0.18
1063-15	0.00	0.57	0.29	0.85	10.33	4.55	0.44	0.19
1063-16	0.00	0.43	0.20	0.60	12.05	4.66	0.39	0.13
1063-17	0.00	0.77	0.21	0.97	10.29	5.76	0.56	0.17

Table 8-b: 1063 (65 µm < x < 43 µm)

	Sequential Fe Extraction				Total Digest		Ratio	
Lab Sample Name (65 µm<x <43 µm)	Na Acetate Fe (wt%)	Dithionite Fe (wt%)	Oxalate Fe (wt%)	Total Reactive Fe (wt%)	Al Total (wt%)	Fe Total (wt%)	Fe_T/Al	Fe_{HR}/Fe_T
1063-1	0.03	0.40	0.27	0.70	6.02	3.19	0.53	0.22
1063-2	0.04	0.47	0.32	0.82	6.53	3.36	0.51	0.24
1063-3	0.01	0.41	0.29	0.72	5.48	3.15	0.57	0.23
1063-4	0.02	0.44	0.31	0.77	6.51	3.19	0.49	0.24
1063-5	0.03	0.50	0.26	0.79	5.10	2.79	0.55	0.28
1063-6	0.01	0.51	0.27	0.79	5.58	3.17	0.57	0.25
1063-7	0.02	0.46	0.41	0.90	5.83	3.16	0.54	0.28
1063-8	0.02	0.93	0.45	1.41	7.57	4.59	0.61	0.31
1063-9	0.01	0.37	0.36	0.74	7.52	4.23	0.56	0.18
1063-10	0.03	0.59	0.40	1.01	8.84	4.22	0.48	0.24
1063-11	0.04	0.55	0.30	0.90	8.75	4.47	0.51	0.20
1063-12	0.06	0.52	0.24	0.83	7.68	3.66	0.48	0.23
1063-13	0.04	0.48	0.34	0.85	8.65	4.60	0.53	0.19
1063-14	0.08	0.53	0.24	0.84	8.45	4.05	0.48	0.21
1063-15	0.08	0.59	0.29	0.97	8.32	4.15	0.50	0.23
1063-16	0.04	0.48	0.33	0.85	7.49	4.02	0.54	0.21
1063-17	0.08	0.47	0.35	0.90	6.69	4.40	0.66	0.20

Table 8-c: Site 1063 (<43µm)

	Sequential Fe Extraction				Total Digest		Ratio	
Lab Sample Name (<43 µm)	Na Acetate Fe (wt%)	Dithionite Fe (wt%)	Oxalate Fe (wt%)	Total Reactive Fe (wt%)	Al Total (wt%)	Fe Total (wt%)	Fe_T/Al	Fe_{HR}/Fe_T
1063-1	0.03	0.25	0.32	0.61	5.81	3.07	0.53	0.20
1063-2	0.06	0.45	0.29	0.80	5.77	3.32	0.58	0.24
1063-3	0.05	0.36	0.29	0.70	6.31	3.37	0.53	0.21
1063-4	0.02	0.40	0.29	0.72	6.01	3.27	0.54	0.22
1063-5	0.04	0.31	0.40	0.75	5.50	3.05	0.55	0.25
1063-6	0.02	1.14	0.40	1.55	5.20	3.17	0.61	0.49
1063-7	0.02	0.55	0.43	1.00	7.14	3.48	0.49	0.29
1063-8	0.03	0.63	0.45	1.11	8.30	4.53	0.55	0.24
1063-9	0.05	0.29	0.37	0.71	7.71	4.17	0.54	0.17
1063-10	0.05	0.41	0.37	0.83	8.01	3.79	0.47	0.22
1063-11	0.05	0.44	0.40	0.88	7.84	4.15	0.53	0.21
1063-12	0.07	0.36	0.36	0.79	6.87	3.94	0.57	0.20
1063-13	0.05	0.31	0.37	0.73	7.03	4.12	0.59	0.18
1063-14	0.08	0.45	0.29	0.81	7.91	4.05	0.51	0.20
1063-15	0.09	0.42	0.42	0.92	8.02	4.36	0.54	0.21
1063-16	0.04	0.41	0.48	0.94	7.72	3.59	0.46	0.26
1063-17	0.14	0.42	0.35	0.92	7.70	4.26	0.55	0.22

Table 9-a: Site 659 (>0.65 µm)

	Sequential Fe Extraction				Total Digest		Ratio	
Lab Sample Name (>0.65 µm)	Na Acetate Fe (wt%)	Dithionite Fe (wt%)	Oxalate Fe (wt%)	Total Reactive Fe (wt%)	Al Total (wt%)	Fe Total (wt%)	Fe_T/Al	Fe_{HR}/Fe_T
659-1	0.10	0.23	0.13	0.46	5.19	2.14	0.41	0.21
659-2	0.06	0.33	0.21	0.60	5.43	1.96	0.36	0.31
659-3	0.03	0.26	0.25	0.54	6.39	2.05	0.32	0.26
659-4	0.04	0.42	0.29	0.76	6.52	2.65	0.41	0.29
659-5	0.03	0.27	0.13	0.44	5.93	2.16	0.37	0.20
659-6	0.11	0.07	0.08	0.25	5.08	1.87	0.37	0.14
659-7	0.04	0.32	0.20	0.56	6.40	2.44	0.38	0.23
659-8	0.01	0.26	0.17	0.44	8.18	2.64	0.32	0.17
659-9	0.10	0.06	0.08	0.24	1.39	0.61	0.44	0.39
659-10	0.13	0.22	0.15	0.50	2.04	1.01	0.49	0.50
659-11	0.12	0.13	0.12	0.37	4.95	1.80	0.36	0.21
659-12	0.14	0.05	0.09	0.29	2.24	0.87	0.39	0.34
659-13	0.14	0.10	0.12	0.36	3.90	1.40	0.36	0.26
659-14	0.05	0.11	0.12	0.29	6.06	2.30	0.38	0.12
659-15	0.10	0.18	0.08	0.36	3.91	1.79	0.46	0.20
659-16	0.18	0.04	0.06	0.28	2.82	1.05	0.37	0.27
659-17	0.12	0.04	0.04	0.21	2.19	0.86	0.39	0.24

Table 9-b: 659 (65 µm < x < 43 µm)

	Sequential Fe Extraction				Total Digest		Ratio	
Lab Sample Name (65 µm<x <43 µm)	Na Acetate Fe (wt%)	Dithionite Fe (wt%)	Oxalate Fe (wt%)	Total Reactive Fe (wt%)	Al Total (wt%)	Fe Total (wt%)	Fe_T/Al	Fe_{HR}/Fe_T
659-1	0.00	0.28	0.08	0.35	2.98	1.52	0.51	0.23
659-2	0.00	0.32	0.21	0.52	3.65	1.78	0.49	0.29
659-3	0.00	0.33	0.23	0.56	4.04	1.62	0.40	0.34
659-4	0.00	0.38	0.42	0.80	4.05	2.36	0.58	0.34
659-5	0.00	0.30	0.18	0.48	3.94	1.79	0.45	0.27
659-6	0.00	0.21	0.10	0.32	0.39	0.17	0.43	1.88
659-7	0.00	0.33	0.13	0.45	4.15	2.13	0.51	0.21
659-8	0.00	0.20	0.17	0.37	5.19	2.38	0.46	0.16
659-9	0.02	0.13	0.07	0.23	1.45	0.99	0.68	0.23
659-10	0.00	0.13	0.08	0.20	1.41	0.91	0.65	0.22
659-11	0.05	0.25	0.14	0.44	3.22	1.64	0.51	0.27
659-12	0.01	0.13	0.12	0.27	2.02	1.05	0.52	0.25
659-13	0.02	0.16	0.07	0.25	2.45	1.25	0.51	0.20
659-14	0.01	0.14	0.13	0.28	4.03	1.98	0.49	0.14
659-15	0.02	0.15	0.11	0.29	2.76	1.76	0.64	0.16
659-16	0.02	0.09	0.03	0.15	1.33	0.73	0.55	0.20
659-17	0.01	0.06	0.02	0.09	2.25	0.94	0.42	0.09

Table 9-c: Site 659 (<43µm)

	Sequential Fe Extraction				Total Digest		Ratio	
Lab Sample Name (<43 µm)	Na Acetate Fe (wt%)	Dithionite Fe (wt%)	Oxalate Fe (wt%)	Total Reactive Fe (wt%)	Al Total (wt%)	Fe Total (wt%)	Fe_T/Al	Fe_{HR}/Fe_T
659-1	0.00	0.40	0.12	0.51	2.99	1.50	0.50	0.34
659-2	0.00	0.34	0.16	0.49	3.16	1.63	0.52	0.30
659-3	0.00	0.38	0.31	0.69	4.19	2.03	0.48	0.34
659-4	0.00	0.38	0.48	0.86	4.33	2.38	0.55	0.36
659-5	0.00	0.32	0.24	0.55	3.56	1.84	0.52	0.30
659-6	0.00	0.27	0.22	0.48	3.90	1.81	0.46	0.27
659-7	0.01	0.29	0.23	0.53	4.73	2.17	0.46	0.24
659-8	0.00	0.27	0.16	0.43	4.61	2.14	0.46	0.20
659-9	0.01	0.13	0.05	0.19	1.39	1.01	0.72	0.19
659-10	0.01	0.14	0.05	0.20	1.45	0.97	0.67	0.21
659-11	0.02	0.22	0.16	0.41	2.92	1.73	0.59	0.27
659-12	0.00	0.13	0.09	0.23	2.11	1.19	0.57	0.19
659-13	0.04	0.13	0.14	0.30	2.61	1.36	0.52	0.22
659-14	0.02	0.15	0.08	0.25	3.51	1.92	0.55	0.13
659-15	0.05	0.38	0.10	0.53	2.92	2.01	0.69	0.26
659-16	0.03	0.08	0.04	0.15	1.37	0.79	0.58	0.19
659-17	0.04	0.08	0.05	0.16	2.16	1.05	0.49	0.16

Table 10-a: Site 1074 (>0.65 µm)

	Sequential Fe Extraction				Total Digest		Ratio	
Lab Sample Name (>0.65 µm)	Na Acetate Fe (wt%)	Dithionite Fe (wt%)	Oxalate Fe (wt%)	Total Reactive Fe (wt%)	Al Total (wt%)	Fe Total (wt%)	Fe_T/Al	Fe_{HR}/Fe_T
1074-1	0.00	0.52	0.16	0.64	2.91	1.59	0.55	0.40
1074-2	0.00	0.42	0.15	0.52	2.18	1.26	0.58	0.41
1074-3	0.00	0.56	0.24	0.74	4.69	2.56	0.55	0.29
1074-4	0.00	0.43	0.31	0.69	4.87	2.26	0.46	0.31
1074-5	0.00	0.79	0.30	1.04	6.57	3.53	0.54	0.29
1074-6	0.00	0.82	0.59	1.36	8.67	4.38	0.50	0.31
1074-7	0.00	0.85	0.19	0.97	5.12	2.81	0.55	0.35
1074-8	0.00	0.62	0.23	0.80	5.29	2.57	0.49	0.31
1074-9	0.00	0.46	0.31	0.72	4.08	2.36	0.58	0.31

Table 10-b: 1074 (65 µm < x < 43 µm)

	Sequential Fe Extraction				Total Digest		Ratio	
Lab Sample Name (65 µm<x <43 µm)	Na Acetate Fe (wt%)	Dithionite Fe (wt%)	Oxalate Fe (wt%)	Total Reactive Fe (wt%)	Al Total (wt%)	Fe Total (wt%)	Fe_T/Al	Fe_{HR}/Fe_T
1074-1	0.00	0.52	0.12	0.59	1.78	1.29	0.72	0.46
1074-2	0.00	0.45	0.17	0.55	1.95	1.38	0.71	0.40
1074-3	0.00	0.57	0.25	0.75	2.98	2.08	0.70	0.36
1074-4	0.00	0.50	0.28	0.72	2.63	1.95	0.74	0.37
1074-5	0.00	0.90	0.34	1.18	4.52	2.90	0.64	0.41
1074-6	0.00	0.71	0.38	1.12	4.87	3.49	0.72	0.32
1074-7	0.00	0.77	0.25	0.98	3.25	2.36	0.73	0.42
1074-8	0.00	0.67	0.23	0.84	2.61	2.05	0.79	0.41
1074-9	0.00	0.73	0.25	0.93	2.63	1.81	0.69	0.51

Table 10-c: Site 1074 (<43µm)

	Sequential Fe Extraction				Total Digest		Ratio	
Lab Sample Name (<43 µm)	Na Acetate Fe (wt%)	Dithionite Fe (wt%)	Oxalate Fe (wt%)	Total Reactive Fe (wt%)	Al Total (wt%)	Fe Total (wt%)	Fe_T/Al	Fe_{HR}/Fe_T
1074-1	0.00	0.55	0.12	0.62	1.72	1.28	0.74	0.48
1074-2	0.00	0.36	0.12	0.42	1.60	1.20	0.75	0.35
1074-3	0.00	0.83	0.37	1.13	3.39	2.20	0.65	0.51
1074-4	0.00	0.72	0.36	1.01	3.06	2.13	0.70	0.47
1074-5	0.00	0.89	0.33	1.14	4.05	2.77	0.68	0.41
1074-6	0.00	0.88	0.68	1.50	5.44	3.32	0.61	0.45
1074-7	0.00	0.65	0.31	0.89	3.28	2.31	0.70	0.39
1074-8	0.00	0.63	0.28	0.84	3.33	2.15	0.64	0.39
1074-9	0.00	0.61	0.22	0.76	2.62	1.96	0.75	0.39

Table 11-Average of the values by grain size distribution

Table 11-a: 1091

1091	Sequential Fe Extraction				Total Digest		Ratio	
Sample Grain Size	Na Acetate Fe (wt%)	Dithionite Fe (wt%)	Oxalate Fe (wt%)	Total Reactive Fe (wt%)	Al Total (wt%)	Fe Total (wt%)	Fe_T/Al	Fe_{HR}/Fe_T
>0.65 µm	0.01	0.09	0.08	0.18	2.43	1.88	0.80	0.10
65 µm<x<43 µm	0.01	0.08	0.07	0.17	2.74	2.03	0.74	0.08
<43 µm	0.01	0.10	0.08	0.20	3.00	2.11	0.70	0.11
Average	0.01	0.09	0.08	0.18	2.72	2.01	0.75	0.10

Table 11-b: 1062

1062	Sequential Fe Extraction				Total Digest		Ratio	
Sample Grain Size	Na Acetate Fe (wt%)	Dithionite Fe (wt%)	Oxalate Fe (wt%)	Total Reactive Fe (wt%)	Al Total (wt%)	Fe Total (wt%)	Fe_T/Al	Fe_{HR}/Fe_T
>0.65 µm	0.04	0.12	0.30	0.45	5.20	3.82	0.77	0.12
65 µm<x<43 µm	0.01	0.10	0.17	0.28	7.31	3.80	0.55	0.09
<43 µm	0.03	0.07	0.18	0.28	6.55	3.58	0.57	0.08
Average	0.03	0.10	0.21	0.34	6.35	3.73	0.63	0.10

Table 11-c: 1063

1063	Sequential Fe Extraction				Total Digest		Ratio	
Sample Grain Size	Na Acetate Fe (wt%)	Dithionite Fe (wt%)	Oxalate Fe (wt%)	Total Reactive Fe (wt%)	Al Total (wt%)	Fe Total (wt%)	Fe_T/Al	Fe_{HR}/Fe_T
>0.65 µm	0.01	0.54	0.24	0.76	10.04	4.48	0.45	0.17
65 µm<x<43 µm	0.04	0.51	0.32	0.87	7.12	3.79	0.54	0.23
<43 µm	0.05	0.45	0.37	0.87	6.99	3.75	0.54	0.24
Average	0.03	0.50	0.31	0.83	8.05	4.01	0.51	0.21

Table 11-d: 659

659	Sequential Fe Extraction				Total Digest		Ratio	
Sample Grain Size	Na Acetate Fe (wt%)	Dithionite Fe (wt%)	Oxalate Fe (wt%)	Total Reactive Fe (wt%)	Al Total (wt%)	Fe Total (wt%)	Fe_T/Al	Fe_{HR}/Fe_T
>0.65 µm	0.09	0.18	0.14	0.41	4.63	1.74	0.39	0.25
65 µm<x<43 µm	0.01	0.21	0.14	0.35	2.90	1.47	0.52	0.32
<43 µm	0.01	0.24	0.16	0.41	3.05	1.62	0.55	0.25
Average	0.04	0.21	0.14	0.39	3.53	1.61	0.48	0.27

Table 11-e: 1074

1074	Sequential Fe Extraction				Total Digest		Ratio	
Sample Grain Size	Na Acetate Fe (wt%)	Dithionite Fe (wt%)	Oxalate Fe (wt%)	Total Reactive Fe (wt%)	Al Total (wt%)	Fe Total (wt%)	Fe_T/Al	Fe_{HR}/Fe_T
>0.65 µm	0.00	0.61	0.28	0.83	4.93	2.59	0.53	0.33
65 µm<x<43 µm	0.00	0.65	0.25	0.85	3.03	2.15	0.71	0.41
<43 µm	0.00	0.68	0.31	0.92	3.17	2.15	0.69	0.43
Average	0.00	0.64	0.28	0.87	3.71	2.29	0.65	0.39

Table 12: Average Fe_{HR} distribution from each site.

Sequential Fe Extraction (% Fe)			
Sites	Na-Acetate	Dithionite	Oxalate
1091	6.7	51.0	42.3
1062	8.2	28.3	36.7
1063	3.8	59.9	37.2
659	9.7	53.9	36.7
1074	0.0	74.2	32.2
Average	5.7	53.5	37.0

References

Andersen, K. K., A. Armengaud, and C. Genthon (1998), Atmospheric dust under glacial and interglacial conditions, *Geophysical Research Letters*, *25*(13), 2281-2284.

Arimoto, R., R. A. Duce, B. J. Ray, and U. Tomza (2003), Dry deposition of trace elements to the western North Atlantic, *Global biogeochemical cycles*, *17*(1).

Arrigo, K. R. (2005), Marine microorganisms and global nutrient cycles, *Nature*, *437*(7057), 349-355.

Aumont, O., E. Maier□Reimer, S. Blain, and P. Monfray (2003), An ecosystem model of the global ocean including Fe, Si, P colimitations, *Global Biogeochemical Cycles*, *17*(2).

Bacon, M. P., and J. N. Rosholt (1982), Accumulation rates of Th-230, Pa-231, and some transition metals on the Bermuda Rise, *Geochimica et Cosmochimica Acta*, *46*(4), 651-666.

Baker, A. R., and T. D. Jickells (2006), Mineral particle size as a control on aerosol iron solubility, *Geophysical Research Letters*, *33*(17).

Baker, A. R., S. D. Kelly, K. F. Biswas, M. Witt, and T. D. Jickells (2003), Atmospheric deposition of nutrients to the Atlantic Ocean, *Geophysical Research Letters*, *30*(24).

Balsam, W. L., B. L. Otto□Bliesner, and B. C. Deaton (1995), Modern and last glacial maximum eolian sedimentation patterns in the Atlantic Ocean interpreted from sediment iron oxide content, *Paleoceanography*, *10*(3), 493-507.

Barbeau, K. (2006), Photochemistry of organic iron (III) complexing ligands in oceanic systems, *Photochemistry and Photobiology*, *82*(6), 1505-1516.

Benner, S. G., C. M. Hansel, B. W. Wielinga, T. M. Barber, and S. Fendorf (2002), Reductive dissolution and biomineralization of iron hydroxide under dynamic flow conditions, *Environmental science & technology*, *36*(8), 1705-1711.

Bergquist, B. A., and E. A. Boyle (2006), Dissolved iron in the tropical and subtropical Atlantic Ocean, *Global Biogeochemical Cycles*, *20*(1).

Berman-Frank, I., J. T. Cullen, Y. Shaked, R. M. Sherrell, and P. G. Falkowski (2001),

Iron availability, cellular iron quotas, and nitrogen fixation in Trichodesmium, *Limnology and Oceanography*, *46*(6), 1249-1260.

Berner, R. A. (1969), Migration of iron and sulfur within anaerobic sediments during early diagenesis, *American Journal of Science*, *267*(1), 19-42.

Berner, R. A. (1970), Sedimentary pyrite formation, *American Journal of Science*, *268*(1), 1-23.

Blott, S. J., and K. Pye (2001), GRADISTAT: a grain size distribution and statistics package for the analysis of unconsolidated sediments, *Earth surface processes and Landforms*, *26*(11), 1237-1248.

Boyd, P. W., A. J. Watson, C. S. Law, E. R. Abraham, T. Trull, R. Murdoch, D. C. E. Bakker, A. R. Bowie, K. O. Buesseler, and H. Chang (2000), A mesoscale phytoplankton bloom in the polar Southern Ocean stimulated by iron fertilization, *Nature*, *407*(6805), 695-702.

Boyd, P. W., C. S. Law, C. S. Wong, Y. Nojiri, A. Tsuda, M. Levasseur, S. Takeda, R. Rivkin, P. J. Harrison, and R. Strzepek (2004), The decline and fate of an iron-induced subarctic phytoplankton bloom, *Nature*, *428*(6982), 549-553.

Brimblecombe, P. (1996), *Air composition and chemistry*, Cambridge University Press.

Broecker, W. S. (1982), Ocean chemistry during glacial time, *Geochimica et Cosmochimica Acta*, *46*(10), 1689-1705.

Canfield, D. E., R. Raiswell, J. T. Westrich, C. M. Reaves, and R. A. Berner (1986), The use of chromium reduction in the analysis of reduced inorganic sulfur in sediments and shales, *Chemical Geology*, *54*(1), 149-155.

Channell, J. E. T., D. A. Hodell, and J. H. Curtis (2012), ODP Site 1063 (Bermuda Rise) revisited: oxygen isotopes, excursions and paleointensity in the Brunhes Chron, *Geochemistry, Geophysics, Geosystems*, *13*(2).

Chen, Y., and R. L. Siefert (2004), Seasonal and spatial distributions and dry deposition fluxes of atmospheric total and labile iron over the tropical and subtropical North Atlantic Ocean, *Journal of Geophysical Research: Atmospheres (1984–2012)*, *109*(D9).

Chester, R., H. Elderfield, J. J. Griffin, L. R. Johnson, and R. C. Padgham (1972), Eolian dust along the eastern margins of the Atlantic Ocean, *Marine Geology*, *13*(2), 91-105.

Claquin, T., M. Schulz, and Y. J. Balkanski (1999), Modeling the mineralogy of atmospheric dust sources, *Journal of Geophysical Research: Atmospheres (1984–2012)*, *104*(D18), 22243-22256.

Coale, K. H., K. S. Johnson, S. E. Fitzwater, R. M. Gordon, S. Tanner, F. P. Chavez, L. Ferioli, C. Sakamoto, P. Rogers, and F. Millero (1996), A massive phytoplankton bloom induced by an ecosystem-scale iron fertilization experiment in the equatorial Pacific Ocean.

Conway, T. M., and S. G. John (2014), Quantification of dissolved iron sources to the North Atlantic Ocean, *Nature*, *511*(7508), 212-215.

De Vitre, R., B. Sulzberger, and J. Buffle (1993), Transformations of iron at redox boundaries, *Chemical and Biological Regulation of Aquatic Systems*, 89-135.

Desboeufs, K. V., R. Losno, and J.-L. Colin (2001), Factors influencing aerosol solubility during cloud processes, *Atmospheric Environment*, *35*(20), 3529-3537.

Duce, R. A., and N. W. Tindale (1991), Atmospheric transport of iron and its deposition in the ocean, *Limnology and Oceanography*, *36*(8), 1715-1726.

Erickson, D. J., J. L. Hernandez, P. Ginoux, W. W. Gregg, C. McClain, and J. Christian (2003), Atmospheric iron delivery and surface ocean biological activity in the Southern Ocean and Patagonian region, *Geophysical Research Letters*, *30*(12).

Eshel, G., G. J. Levy, U. Mingelgrin, and M. J. Singer (2004), Critical evaluation of the use of laser diffraction for particle-size distribution analysis, *Soil Science Society of America Journal*, *68*(3), 736-743.

Etourneau, J., C. Ehlert, M. Frank, P. Martinez, and R. Schneider (2012), Contribution of changes in opal productivity and nutrient distribution in the coastal upwelling systems to Late Pliocene/Early Pleistocene climate cooling, *Climate of the Past*, *8*(5), 1435-1445.

Falkowski, P. G. (1997), Evolution of the nitrogen cycle and its influence on the biological sequestration of CO 2 in the ocean, *Nature*, *387*(6630), 272-275.

Fan, S. M., W. J. Moxim, and H. Levy (2006), Aeolian input of bioavailable iron to the ocean, *Geophysical research letters*, *33*(7).

Farrera, I., S. P. Harrison, I. C. Prentice, G. Ramstein, J. Guiot, P. J. Bartlein, R. Bonnefille, M. Bush, W. Cramer, and U. Von Grafenstein (1999), Tropical climates at the Last Glacial Maximum: a new synthesis of terrestrial

palaeoclimate data. I. Vegetation, lake-levels and geochemistry, *Climate Dynamics*, *15*(11), 823-856.

Franz, S. O., and R. Tiedemann (2002), Depositional changes along the Blake Bahama Outer Ridge deep water transect during marine isotope stages 8 to 10– links to the Deep Western Boundary Current, *Marine geology*, *189*(1), 107-122.

Fung, I. Y., S. K. Meyn, I. Tegen, S. C. Doney, J. G. John, and J. K. B. Bishop (2000), Iron Supply and demand in the upper ocean, *Global Biogeochemical Cycles*, *14*(1), 281-295.

Gao, Y., Y. J. Kaufman, D. Tanre, D. Kolber, and P. G. Falkowski (2001), Seasonal distributions of aeolian iron fluxes to the global ocean, *Geophysical Research Letters*, *28*(1), 29-32.

Gersonde, R., D. A. Hodell, and P. Blum (1999), 1. LEG 177 Summary: Southern ocean Paeoceanoghraphy 1.
.

Gibbs, M. T., and L. R. Kump (1994), Global chemical erosion during the last glacial maximum and the present: sensitivity to changes in lithology and hydrology, *Paleoceanography*, *9*(4), 529-543.

Gibbs, S. J., J. R. Young, T. J. Bralower, and N. J. Shackleton (2005), Nannofossil evolutionary events in the mid-Pliocene: an assessment of the degree of synchrony in the extinctions of Reticulofenestra pseudoumbilicus and Sphenolithus abies, *Palaeogeography, Palaeoclimatology, Palaeoecology*, *217*(1), 155-172.

Gregg, W. W., M. E. Conkright, P. Ginoux, J. E. O'Reilly, and N. W. Casey (2003), Ocean primary production and climate: Global decadal changes, *Geophysical Research Letters*, *30*(15).

Grigorov, I., R. B. Pearce, and A. E. S. Kemp (2002), Southern Ocean laminated diatom ooze: mat deposits and potential for palaeo-flux studies, ODP leg 177, Site 1093, *Deep Sea Research Part II: Topical Studies in Oceanography*, *49*(16), 3391-3407.

Gruetzner, J., L. Giosan, S. O. Franz, R. Tiedemann, E. Cortijo, W. P. Chaisson, R. D. Flood, S. Hagen, L. D. Keigwin, and S. Poli (2002), Astronomical age models for Pleistocene drift sediments from the western North Atlantic (ODP Sites 1055–1063), *Marine Geology*, *189*(1), 5-23.

Hand, J. L., N. M. Mahowald, Y. Chen, R. L. Siefert, C. Luo, A. Subramaniam, and I.

Fung (2004), Estimates of atmospheric processed soluble iron from observations and a global mineral aerosol model: Biogeochemical implications, *Journal of Geophysical Research: Atmospheres (1984–2012)*, *109*(D17).

Harrison, S. P., K. E. Kohfeld, C. Roelandt, and T. Claquin (2001), The role of dust in climate changes today, at the last glacial maximum and in the future, *Earth-Science Reviews*, *54*(1), 43-80.

Hassler, C. S., V. Schoemann, C. M. Nichols, E. C. V. Butler, and P. W. Boyd (2011), Saccharides enhance iron bioavailability to Southern Ocean phytoplankton, *Proceedings of the National Academy of Sciences*, *108*(3), 1076-1081.

Haug, G. H., and R. Tiedemann (1998), Effect of the formation of the Isthmus of Panama on Atlantic Ocean thermohaline circulation, *Nature*, *393*(6686), 673-676.

Heiri, O., A. F. Lotter, and G. Lemcke (2001), Loss on ignition as a method for estimating organic and carbonate content in sediments: reproducibility and comparability of results, *Journal of paleolimnology*, *25*(1), 101-110.

Hirano, S., Y. Ogawa, and K. Kawamura 1. Deformation of Unlimited Sediments in an Early Stage of the Compaction Process deduced from Microtextures and Magnetic Fabrics: ODP LEG 174B, HOLE 1074A1.

Hunter, K. A., and P. W. Boyd (2007), Iron-binding ligands and their role in the ocean biogeochemistry of iron, *Environmental Chemistry*, *4*(4), 221-232.

Jickells, T. D., Z. S. An, K. K. Andersen, A. R. Baker, G. Bergametti, N. Brooks, J. J. Cao, P. W. Boyd, R. A. Duce, and K. A. Hunter (2005), Global iron connections between desert dust, ocean biogeochemistry, and climate, *science*, *308*(5718), 67-71.

Jimenez, J. L., M. R. Canagaratna, N. M. Donahue, A. S. H. Prevot, Q. Zhang, J. H. Kroll, P. F. DeCarlo, J. D. Allan, H. Coe, and N. L. Ng (2009), Evolution of organic aerosols in the atmosphere, *Science*, *326*(5959), 1525-1529.

Johnson, K. S., R. M. Gordon, and K. H. Coale (1997), What controls dissolved iron concentrations in the world ocean?, *Marine Chemistry*, *57*(3), 137-161.

Jolly, D., and A. Haxeltine (1997), Effect of low glacial atmospheric CO2 on tropical African montane vegetation, *Science*, *276*(5313), 786-788.

Journet, E., K. V. Desboeufs, S. Caquineau, and J. L. Colin (2008), Mineralogy as a critical factor of dust iron solubility, *Geophysical Research Letters*, *35*(7).

Keigwin, L. D., and G. A. Jones (1989), Glacial-Holocene stratigraphy, chronology, and paleoceanographic observations on some North Atlantic sediment drifts, *Deep Sea Research Part A. Oceanographic Research Papers*, *36*(6), 845-867.

Kemp, A. E. S., I. Grigorov, R. B. Pearce, and A. C. N. Garabato (2010), Migration of the Antarctic Polar Front through the mid-Pleistocene transition: evidence and climatic implications, *Quaternary Science Reviews*, *29*(17), 1993-2009.

Kieber, R. J., K. Williams, J. D. Willey, S. Skrabal, and G. B. Avery (2001), Iron speciation in coastal rainwater: concentration and deposition to seawater, *Marine chemistry*, *73*(2), 83-95.

Kleiven, H. F., and E. Jansen (2003), 12. Data Report: Early-Mid-Pleistocene Oxygen Isotope Stratigraphy from the Atlantic Sector of the Southern Ocean: ODP Leg 177 Sites 1094 and 1091.

Kohfeld, K. E., and S. P. Harrison (2001), DIRTMAP: the geological record of dust, *Earth-Science Reviews*, *54*(1), 81-114.

Kumar, N., R. F. Anderson, R. A. Mortlock, P. N. Froelich, P. Kubik, B. Dittrich Hannen, and M. Suter (1995), Increased biological productivity and export production in the glacial Southern Ocean, *Nature*, *378*(6558), 675-680.

Leventhal, J., and C. Taylor (1990), Comparison of methods to determine degree of pyritization, *Geochimica et Cosmochimica Acta*, *54*(9), 2621-2625.

Loizeau, J. L., D. Arbouille, S. Santiago, and J. P. Vernet (1994), Evaluation of a wide range laser diffraction grain size analyser for use with sediments, *Sedimentology*, *41*(2), 353-361.

Lund, S. P., T. Williams, G. D. Acton, B. Clement, and M. Okada (2001), 10. Brunhes Chron Magnetic Field Excursions Recovered from Leg 172 Sediments.

Luo, C., N. M. Mahowald, N. Meskhidze, Y. Chen, R. L. Siefert, A. R. Baker, and A. M. Johansen (2005), Estimation of iron solubility from observations and a global aerosol model, *Journal of Geophysical Research: Atmospheres (1984–2012)*, *110*(D23).

Lyons, T. W., and S. Severmann (2006), A critical look at iron paleoredox proxies: new insights from modern euxinic marine basins, *Geochimica et Cosmochimica Acta*, *70*(23), 5698-5722.

Mackie, D. S., P. W. Boyd, K. A. Hunter, and G. H. McTainsh (2005), Simulating the

cloud processing of iron in Australian dust: pH and dust concentration, *Geophysical Research Letters*, *32*(6).

Mahowald, N., K. Kohfeld, M. Hansson, Y. Balkanski, S. P. Harrison, I. C. Prentice, M. Schulz, and H. Rodhe (1999), Dust sources and deposition during the last glacial maximum and current climate: A comparison of model results with paleodata from ice cores and marine sediments, *Journal of Geophysical Research: Atmospheres (1984–2012)*, *104*(D13), 15895-15916.

Mahowald, N., T. D. Jickells, A. R. Baker, P. Artaxo, C. R. Benitez□Nelson, G. Bergametti, T. C. Bond, Y. Chen, D. D. Cohen, and B. Herut (2008), Global distribution of atmospheric phosphorus sources, concentrations and deposition rates, and anthropogenic impacts, *Global Biogeochemical Cycles*, *22*(4).

Mahowald, N. M., A. R. Baker, G. Bergametti, N. Brooks, R. A. Duce, T. D. Jickells, N. Kubilay, J. M. Prospero, and I. Tegen (2005), Atmospheric global dust cycle and iron inputs to the ocean, *Global biogeochemical cycles*, *19*(4).

Mahowald, N. M., S. Engelstaedter, C. Luo, A. Sealy, P. Artaxo, C. Benitez-Nelson, S. Bonnet, Y. Chen, P. Y. Chuang, and D. D. Cohen (2009), Atmospheric iron deposition: Global distribution, variability, and human perturbations*, *Marine Science*, *1*.

Martin, J. H. (1990), Glacial□interglacial CO2 change: The iron hypothesis, *Paleoceanography*, *5*(1), 1-13.

Martin, J. H., K. H. Coale, K. S. Johnson, S. E. Fitzwater, R. M. Gordon, S. J. Tanner, C. N. Hunter, V. A. Elrod, J. L. Nowicki, and T. L. Coley (1994), Testing the iron hypothesis in ecosystems of the equatorial Pacific Ocean.

Mienert, J., and P. Schultheiss (1986), 23. Pusical Properties of sedimentary Envoroments in oceanic High (Site 658) and Low (659) Productivity Zones 1, paper presented at Proceedings of the Ocean Drilling Program: Scientific results, The Program.

Moore, C. M., M. M. Mills, E. P. Achterberg, R. J. Geider, J. LaRoche, M. I. Lucas, E. L. McDonagh, X. Pan, A. J. Poulton, and M. J. A. Rijkenberg (2009), Large-scale distribution of Atlantic nitrogen fixation controlled by iron availability, *Nature Geoscience*, *2*(12), 867-871.

Moore, J. K., and O. Braucher (2008), Sedimentary and mineral dust sources of dissolved iron to the world ocean, *Biogeosciences*, *5*(3).

Moore, J. K., S. C. Doney, and K. Lindsay (2004), Upper ocean ecosystem dynamics

and iron cycling in a global three□dimensional model, *Global Biogeochemical Cycles*, *18*(4).

Moore, J. K., S. C. Doney, D. M. Glover, and I. Y. Fung (2001), Iron cycling and nutrient-limitation patterns in surface waters of the World Ocean, *Deep Sea Research Part II: Topical Studies in Oceanography*, *49*(1), 463-507.

Neff, J. C., E. A. Holland, F. J. Dentener, W. H. McDowell, and K. M. Russell (2002), The origin, composition and rates of organic nitrogen deposition: A missing piece of the nitrogen cycle?, *Biogeochemistry*, *57*(1), 99-136.

Ooki, A., J. Nishioka, T. Ono, and S. Noriki (2009), Size dependence of iron solubility of Asian mineral dust particles, *Journal of Geophysical Research: Atmospheres (1984–2012)*, *114*(D3).

Peterson, L. C., G. H. Haug, K. A. Hughen, and U. Röhl (2000), Rapid changes in the hydrologic cycle of the tropical Atlantic during the last glacial, *Science*, *290*(5498), 1947-1951.

Petit, J.-R., J. Jouzel, D. Raynaud, N. I. Barkov, J. M. Barnola, I. Basile, M. Bender, J. Chappellaz, M. Davis, and G. Delaygue (1999), Climate and atmospheric history of the past 420,000 years from the Vostok ice core, Antarctica, *Nature*, *399*(6735), 429-436.

Pokrovsky, O. S., and J. Schott (2002), Iron colloids/organic matter associated transport of major and trace elements in small boreal rivers and their estuaries (NW Russia), *Chemical Geology*, *190*(1), 141-179.

Poulton, S. W., and R. Raiswell (2002), The low-temperature geochemical cycle of iron: from continental fluxes to marine sediment deposition, *American Journal of Science*, *302*(9), 774-805.

Poulton, S. W., and D. E. Canfield (2005), Development of a sequential extraction procedure for iron: implications for iron partitioning in continentally derived particulates, *Chemical Geology*, *214*(3), 209-221.

Prospero, J. M. (1999), Long-range transport of mineral dust in the global atmosphere: Impact of African dust on the environment of the southeastern United States, *Proceedings of the National Academy of Sciences*, *96*(7), 3396-3403.

Pruppacher, H. R., J. D. Klett, and P. K. Wang (1998), Microphysics of clouds and precipitation.

Raiswell, R. (2011), Iceberg-hosted nanoparticulate Fe in the Southern Ocean: mineralogy, origin, dissolution kinetics and source of bioavailable Fe, *Deep Sea Research Part II: Topical Studies in Oceanography*, *58*(11), 1364-1375.

Raiswell, R., and D. E. Canfield (1998), Sources of iron for pyrite formation in marine sediments, *American Journal of Science*, *298*(3), 219-245.

Raiswell, R., and D. E. Canfield (2012), The iron biogeochemical cycle past and present, *Geochemical Perspectives*, *1*(1), 1-2.

Raiswell, R., D. Canfield, and R. Berner (1994), A comparison of iron extraction methods for the determination of degree of pyritisation and the recognition of iron-limited pyrite formation, *Chemical Geology*, *111*(1), 101-110.

Raiswell, R., R. Newton, and P. B. Wignall (2001), An indicator of water-column anoxia: resolution of biofacies variations in the Kimmeridge Clay (Upper Jurassic, UK), *Journal of Sedimentary Research*, *71*(2), 286-294.

Raiswell, R., L. G. Benning, L. Davidson, and M. Tranter (2008), Nanoparticulate bioavailable iron minerals in icebergs and glaciers, *Mineralogical Magazine*, *72*(1), 345-348.

Raiswell, R., M. Tranter, L. G. Benning, M. Siegert, R. De'ath, P. Huybrechts, and T. Payne (2006), Contributions from glacially derived sediment to the global iron (oxyhydr) oxide cycle: implications for iron delivery to the oceans, *Geochimica et Cosmochimica Acta*, *70*(11), 2765-2780.

Rasch, P. J., J. Feichter, K. Law, N. Mahowald, J. Penner, C. Benkowitz, C. Genthon, G. Giannakopoulos, P. Kasibhatla, and D. Koch (2000), An assessment of scavenging and depositon processes in global models: Results of the WCRP Cambridge Workshop of 1995, *J. Geophys. Res*.

Rea, D. K. (1994), The paleoclimatic record provided by eolian deposition in the deep sea: The geologic history of wind, *Reviews of Geophysics*, *32*(2), 159-196.

Reid, J. S., J. E. Kinney, D. L. Westphal, B. N. Holben, E. J. Welton, S. C. Tsay, D. P. Eleuterio, J. R. Campbell, S. A. Christopher, and P. R. Colarco (2003), Analysis of measurements of Saharan dust by airborne and ground□based remote sensing methods during the Puerto Rico Dust Experiment (PRIDE), *Journal of Geophysical Research: Atmospheres (1984–2012)*, *108*(D19).

Rubasinghege, G., R. W. Lentz, M. M. Scherer, and V. H. Grassian (2010), Simulated

atmospheric processing of iron oxyhydroxide minerals at low pH: roles of particle size and acid anion in iron dissolution, *Proceedings of the National Academy of Sciences*, *107*(15), 6628-6633.

Sarnthein, M., J. Thiede, U. Pflaumann, H. Erlenkeuser, D. Fütterer, B. Koopmann, H. Lange, and E. Seibold (1982), Atmospheric and oceanic circulation patterns off Northwest Africa during the past 25 million years, in *Geology of the Northwest African continental margin*, edited, pp. 545-604, Springer.

Sarthou, G., A. R. Baker, S. Blain, E. P. Achterberg, M. Boye, A. R. Bowie, P. Croot, P. Laan, H. J. W. de Baar, and T. D. Jickells (2003), Atmospheric iron deposition and sea-surface dissolved iron concentrations in the eastern Atlantic Ocean, *Deep Sea Research Part I: Oceanographic Research Papers*, *50*(10), 1339-1352.

Schulz, H., U. von Rad, and H. Erlenkeuser (1998), Correlation between Arabian Sea and Greenland climate oscillations of the past 110,000 years, *Nature*, *393*(6680), 54-57.

Shi, Z., M. D. Krom, S. Bonneville, A. R. Baker, T. D. Jickells, and L. G. Benning (2009), Formation of iron nanoparticles and increase in iron reactivity in mineral dust during simulated cloud processing, *Environmental science & technology*, *43*(17), 6592-6596.

Shi, Z., M. D. Krom, T. D. Jickells, S. Bonneville, K. S. Carslaw, N. Mihalopoulos, A. R. Baker, and L. G. Benning (2012), Impacts on iron solubility in the mineral dust by processes in the source region and the atmosphere: A review, *Aeolian Research*, *5*, 21-42.

Shi, Z. B., M. T. Woodhouse, K. S. Carslaw, M. D. Krom, G. W. Mann, A. R. Baker, I. Savov, G. R. Fones, B. Brooks, and N. Drake (2011), Minor effect of physical size sorting on iron solubility of transported mineral dust, *Atmospheric Chemistry and Physics*, *11*(16), 8459-8469.

Siffert, C., and B. Sulzberger (1991), Light-induced dissolution of hematite in the presence of oxalate. A case study, *Langmuir*, *7*(8), 1627-1634.

Spokes, L. J., T. D. Jickells, and B. Lim (1994), Solubilisation of aerosol trace metals by cloud processing: A laboratory study, *Geochimica et Cosmochimica Acta*, *58*(15), 3281-3287.

Talbot, R. W., R. C. Harriss, E. V. Browell, G. L. Gregory, D. I. Sebacher, and S. M. Beck (1986), Distribution and geochemistry of aerosols in the tropical North Atlantic troposphere: Relationship to Saharan dust, *Journal of Geophysical Research: Atmospheres (1984–2012)*, *91*(D4), 5173-5182.

Taylor, A., and J. D. Blum (1995), Relation between soil age and silicate weathering rates determined from the chemical evolution of a glacial chronosequence, *Geology*, *23*(11), 979-982.

Taylor, S. R., and S. M. McLennan (1995), The geochemical evolution of the continental crust, *Reviews of Geophysics*, *33*(2), 241-265.

Tiedemann, R., M. Sarnthein, and N. J. Shackleton (1994), Astronomic timescale for the Pliocene Atlantic δ18O and dust flux records of Ocean Drilling Program Site 659, *Paleoceanography*, *9*(4), 619-638.

Tortell, P. D., M. T. Maldonado, J. Granger, and N. M. Price (1999), Marine bacteria and biogeochemical cycling of iron in the oceans, *FEMS Microbiology Ecology*, *29*(1), 1-11.

Türke, A., W. Bach, and M. S. Mehmood Data report: X-ray fluorescence scanning of sediment cores from Holes U1382B, U1383D, U1384A, and 1074A from the North Pond area, paper presented at Proc. IODP| Volume.

Watson, A. J., D. C. E. Bakker, A. J. Ridgwell, P. W. Boyd, and C. S. Law (2000), Effect of iron supply on Southern Ocean CO2 uptake and implications for glacial atmospheric CO2, *Nature*, *407*(6805), 730-733.

Zender, C. S., H. Bian, and D. Newman (2003), Mineral Dust Entrainment and Deposition (DEAD) model: Description and 1990s dust climatology, *Journal of Geophysical Research: Atmospheres (1984–2012)*, *108*(D14).

Zhu, X. R., J. M. Prospero, and F. J. Millero (1997), Diel variability of soluble Fe (II) and soluble total Fe in North African dust in the trade winds at Barbados, *Journal of Geophysical Research: Atmospheres (1984–2012)*, *102*(D17), 21297-21305.

Ziebis, W., J. McManus, T. Ferdelman, F. Schmidt-Schierhorn, W. Bach, J. Muratli, K. J. Edwards, and H. Villinger (2012), Interstitial fluid chemistry of sediments underlying the North Atlantic gyre and the influence of subsurface fluid flow, *Earth and Planetary Science Letters*, *323*, 79-91.